© 2018 IEEE. Personal use of this material is permitted. Permission from IEEE must be obtained for all other uses, in any current or future media, including reprinting/republishing this material for advertising or promotional purposes, creating new collective works, for resale or redistribution to servers or lists, or reuse of any copyrighted component of this work in other works

Title:
A Coherent Multilayer Simulator of Radargrams Acquired by Radar Sounder Instruments

This paper appears in:
IEEE Transactions on Geoscience and Remote Sensing

Date of Publication:
2018

Author(s):
Christopher Gerekos, Alessandro Tamponi, Leonardo Carrer, Davide Castelletti, Massimo Santoni, Lorenzo Bruzzone

DOI:
10.1109/TGRS.2018.2851020

A Coherent Multilayer Simulator of Radargrams Acquired by Radar Sounder Instruments

Christopher Gerekos, Alessandro Tamponi, Leonardo Carrer, Davide Castelletti, Massimo Santoni, and Lorenzo Bruzzone,

***Abstract*—Reliable electromagnetic simulators are of prime importance for the design of radar sounder instruments and for supporting the subsequent analysis of their data. In this paper we present a coherent, facet method-based simulator that can compute radar echoes from the subsurface of a target area with an arbitrary number of geological layers, thus going beyond the surface-only or the 2-layer descriptions so far implemented in coherent ray-tracing radar sounder simulators. Propagation of fields throughout the subsurface is computed according to Snell's law following a ray-tracing approach. For each ray interacting with the surface, be it a direct reflection or a refracted ray coming from the subsurface, the phase contribution of each facet is calculated through the linear phase approximation, while the total field received at the antenna is computed using Huygen's principle. Validation simulations have been performed against radar data of lunar and martian areas characterized by a multilayer nature, collected by the Lunar Radar Sounder (LRS) instrument of JAXA's Kaguya lunar probe and the Shallow Radar (SHARAD) instrument onboard NASA's Mars Reconnaissance Orbiter, respectively. Results confirm the effectiveness of the proposed simulator.**

I. Introduction

DUE to their unique ability to remotely probe the subsurface of a planetary body, radar sounders are very valuable instruments in the payload of a planetary mission. Planetary radar sounders are usually active, monostatic, nadir-looking instruments working with low-frequency electromagnetic waves, often in the HF or VHF band. Past or present geophysical processes on solid celestial objects often result in stratified terrains, with each layer being characterized by a different dielectric constant. Such discontinuities produce a reflection if hit upon by an incoming electromagnetic wave, which can be measured by the receiver of a radar instrument. Two successful examples of orbital radar sounders are MARSIS (onboard ESA's Mars Express probe) [21], and SHARAD (flown on NASA's Mars Reconnaissance Orbiter) [26], which have been orbiting Mars for many years. Radar sounders have also been successfully used on the Moon, as indicated by the LRS instrument onboard JAXA's Kagyua spacecraft [18]. Currently, two more radar instruments for planetary missions are under development: RIME, onboard ESA's future JUICE spacecraft to Jupiter's icy moons, Ganymede, Europa and Calisto, [3]; and REASON, onboard NASA's upcoming Europa Clipper, targeting the Jovian moon Europa [2]. On Earth, although no orbital radar sounder has been launched so far, many radar sounder instruments have been developed for airborne platforms. Such platforms include the mutli-instrument sounding system for polar research developed by CReSIS [23], the POLARIS instrument of ESA [9], the bistatic radar flown by the British Antarctic Survey [8] and the multimode P-band sounder funded by the Italian Space Agency [20].

However, there are many obstacles to a correct interpretation of radar signals. The major challenges are related to: (i) surface clutter, which is caused by off-nadir echoes arising from terrain topography appearing as deeper features in a given range line, (ii) optical deformations of subsurface features due to the varying indices of refraction of the terrain, and (iii) subsurface clutter. Additionally, complex subsurface features may result in signals that are difficult to interpret. Simulation techniques are very well-suited to address all these issues simultaneously, as they attempt to reproduce the radar response of the the terrain itself (or the portion of it relevant to the considered analysis). The central role that that radar sounder simulators play in both the design of a mission and the subsequent analysis of the acquired data is thus easy to comprehend.

Finite-difference time-domain (FDTD) methods are among the most powerful simulation methods available in the literature. They work by propagating the electromagnetic fields by discrete time-steps in a volume discretized into small, independent 3D cells, and are able to simulate the time-dependant electromagnetic signals with arbitrary bandwidths in arbitrary three-dimensional volumes. When applied to large-scale radar problems, these methods are however extremely demanding in computational resources (see *e.g.* [7]), and many problems simply does not need the range of capabilities offered by FDTD. Ray-tracing simulations are a good compromise between modelling capability and simplicity, and for this reason they have been widely used to support planetary radar missions or airborne radar campaigns (e.g. [25][29]). Methods using ray-tracing can be divided into two categories: incoherent and coherent methods. Incoherent methods place a point in a range line for every echo from the target area, and use a backscattering law to scale its brightness [6][25][29], whereas coherent methods aim to compute the actual electromagnetic field detected by the antenna, based on a given diffraction formula [1][5][10][12][13][17]. As coherent simulators also model the phase information of the radar echo, they can obtain more accurate results.

However, ray-tracing simulators have mostly been developed and used for the analysis of surface clutter only, and to the best of our knowledge, the few techniques being able to

The authors are with the Department of Information Engineering and Computer Science, University of Trento, 38123 Trento, Italy (e-mail: christopher.gerekos@unitn.it; lorenzo.bruzzone@ing.unitn.it).

Accepted on June 15, 2018.

address subsurface descriptions are either incoherent [29] or limited to one subsurface layer [5][12][13]. In [12][13], the authors propose a simulator that treats subsurface echoes by computing the field at each point of the subsurface using the Stratton-Chu integral. While this approach is exact within the limits of the Kirchhoff approximation, it is computationally very intensive (the dimensions of the subsurface layer were restricted in order to keep the simulation time manageable). In [5], several simplifying assumptions are introduced in order to devise a faster method: for a ray impacting the surface, the transmitted wavevector and field are computed according to the laws of classical optics. At the single subsurface layer, the same is done for the reflected wavevector and fields, by taking into account the phase accumulated by the light ray within the subsurface. This field is then used to compute the field at the receiver using Stratton-Chu's integral.

In this paper we present a multilayer coherent radar echo simulator, *i.e.*, a technique being able to treat subsurface targets with an arbitrary number of geological layers and to reproduce how such areas would be imaged by a specific radar instrument. This is done by calculating the electromagnetic field received at the antenna in a coherent way by taking into account all major radar parameters, such as its central frequency, bandwidth, pulse duration, and peak emission power. Propagation of fields throughout the surface and subsurfaces is computed according to Snell's law using a ray-tracing approach, in a way similar to [5]. For each ray interacting with the surface, be it a direct reflection or a refracted ray coming from the subsurface, the phase contribution of each facet is calculated through the linear phase approximation formula [1], while the total field received at the antenna is computed using Huygen's principle. The final signal can then be post-processed in the same way as actual radar data. Such post-processing can include range-compression, focusing, carrier removal, and any algorithm that can enhance the quality of real radar measurements. The simulator has been validated by comparing it against actual radar data from lunar and martian areas characterized by a layered subsurface, using the corresponding digital elevation models (DEMs) and subsurface geoelectrical models. The data have been collected by the Lunar Radar Sounder (LRS) instrument onboard JAXA's Kaguya probe and the Shallow Radar (SHARAD) instrument onboard NASA's Mars Reconnaissance Orbiter (MRO), respectively. The proposed simulator produced results having a very good agreement with the real data.

The proposed algorithm can naturally be used as a system engineering tool for performance assessment in the payload design phase. However, its most interesting application resides in the testing of hypotheses about the subsurface. Indeed, while the surface of a target area can be known if quality DEMs are available, there is no way to acquire such information for the subsurface, and its structure must be inferred from other information sources. The present simulator offers an effective way to test hypothetical subsurface models by showing how a given subsurface would actually appear in the radargram, and compare it to the original radar data of that area.

Due to assumptions and approximations that will be clarified later in the text, the proposed method is better suited to simulate radars on orbital platforms rather than airborne ones, as the altitude is then high enough to make the double-reflection phenomenon irrelevant. Additionally, the simulator will produce more accurate results on low-frequency sounders as it cannot take sub-DEM resolution roughness into account.

This manuscript is structured as follows. Section II presents a review of the state of the art. Section III describes the proposed technique, Section IV presents a reliability and accuracy analysis of the simulator versus its main parameters. Section V presents the experimental results obtained for real data to validate the proposed method. Section VI draws the conclusions of the paper.

II. State-of-the-art of coherent radargram simulators

In this section we briefly recall the main concepts behind coherent radargram simulators.

Harmonic dependence of the fields is always assumed unless otherwise mentioned: $\mathbf{E}(\mathbf{r},t) = Re\left\{\mathbf{E}(\mathbf{r})e^{-i\omega t}\right\}$, and all domains considered are taken to be homogeneous and isotropic. The notations used is the following. Hatted vectors represent versors (*i.e.*, vectors of unit norm). Vectors with an i index represent quantities related to the emitter. For instance, $\mathbf{r_i}$ and $\mathbf{k_i}$ will represent the position of the emitting antenna and the wavevector of the emitted field, respectively. Vectors with an index r will rather are related to the receptor, with, for example, $\mathbf{r_r}$ as the position of the receiving antenna. Lastly $\mathbf{r}'$ rather represents a position on the surface of the target area, which will in our case be a portion of the surface of a planetary body.

A. Huygen's principle and the Stratton-Chu integral

Let us consider an homogeneous and isotropic volume V enclosed by a surface S. The so-called Huygens principle states that the electromagnetic field at any point inside V can be determined knowing the tangential fields on S. Although Huygen's principle is more general, we consider S to be the surface of the planetary body investigated by the radar, or a portion of this surface. Formally, Huygen's principle states that the reflected electric field $\mathbf{E_s}(\mathbf{r})$ at a given point $\mathbf{r}$ is given by [14]

$$\mathbf{E_s}(\mathbf{r}) = \oiint_S d\Sigma' \left\{ i\omega\mu \mathbf{G}(\mathbf{r},\mathbf{r}')\cdot\mathbf{H}_{\parallel}(\mathbf{r}') + \nabla\times\mathbf{G}(\mathbf{r},\mathbf{r}')\cdot\mathbf{E}_{\parallel}(\mathbf{r}') \right\} \tag{1}$$

where $d\Sigma'$ is a surface element on the considered surface S, $\mathbf{E}_{\parallel}(\mathbf{r}') \equiv \hat{\mathbf{n}}(\mathbf{r}')\times\mathbf{E}(\mathbf{r}')$ and $\mathbf{H}_{\parallel}(\mathbf{r}') \equiv \hat{\mathbf{n}}(\mathbf{r}')\times\mathbf{H}(\mathbf{r}')$ are the components of the local tangential electric and magnetic fields at point $\mathbf{r}'$, $\hat{\mathbf{n}}(\mathbf{r}')$ is the local outgoing normal unit vector to the surface. $\mathbf{G}(\mathbf{r},\mathbf{r}')$, the tensorial Green's function, is given by

$$\mathbf{G}(\mathbf{r},\mathbf{r}') = \left[\mathbf{I} + \frac{1}{k^2}\nabla\nabla\right] g(|\mathbf{r}-\mathbf{r}'|) \tag{2}$$

with $\mathbf{I}$ being the identity tensor and

$$g(|\mathbf{r}-\mathbf{r}'|) = \frac{e^{ik|\mathbf{r}-\mathbf{r}'|}}{4\pi|\mathbf{r}-\mathbf{r}'|} \tag{3}$$

being the usual Green's function to the scalar wave equation in three dimensions. Other equivalent forms of Huygens' principle exist in the literature.

We furthermore divide S into a mesh of N facets Δ_α, $S = \{\Delta_\alpha\}_{\alpha=1,\dots,N}$. The shape of those facets can be arbitrary, and does not even need to remain the same across S. In this paper we use right-angled triangles of constant dimensions for simplicity. Computing the total electric field emitted by the surface after being hit upon by an incoming wave thus reduces to a coherent sum of the fields emitted by every facet.

Borrowing the notation of [1] and [14] , we define a local orthonormal basis $\{\hat{\mathbf{k}}_\mathbf{i}, \hat{\mathbf{p}}_\mathbf{i}, \hat{\mathbf{q}}_\mathbf{i}\}$ at point $\mathbf{r}'$ on the surface as follows :

$$\hat{\mathbf{q}}_\mathbf{i} \equiv \frac{\hat{\mathbf{k}}_\mathbf{i} \times \hat{\mathbf{n}}}{|\hat{\mathbf{k}}_\mathbf{i} \times \hat{\mathbf{n}}|} \quad , \quad \hat{\mathbf{p}}_\mathbf{i} \equiv \hat{\mathbf{q}}_\mathbf{i} \times \hat{\mathbf{k}}_\mathbf{i}, \tag{4}$$

where $\hat{\mathbf{n}}$ is the (local) outgoing normal to the surface and $\hat{\mathbf{k}}_\mathbf{i}$ the unit wavevector of the incoming wave. It can then be shown that the "unit fields" $\hat{\mathbf{E}}_\parallel(\mathbf{r}')$ and $\hat{\mathbf{H}}_\parallel(\mathbf{r}')$ at the surface can be written as

$$\begin{aligned}\hat{\mathbf{E}}_\parallel(\mathbf{r}') = \big[&(\hat{\mathbf{e}}_\mathbf{i} \cdot \hat{\mathbf{q}}_\mathbf{i})(\hat{\mathbf{n}} \times \hat{\mathbf{q}}_\mathbf{i})(1 + R^{TE}) \\ &+(\hat{\mathbf{e}}_\mathbf{i} \cdot \hat{\mathbf{p}}_\mathbf{i})(\hat{\mathbf{n}} \cdot \hat{\mathbf{k}}_\mathbf{i})\hat{\mathbf{q}}_\mathbf{i}(1 - R^{TM})\big],\end{aligned} \tag{5}$$

$$\begin{aligned}\hat{\mathbf{H}}_\parallel(\mathbf{r}') = \frac{1}{\eta_i}\big[&-(\hat{\mathbf{e}}_\mathbf{i} \cdot \hat{\mathbf{q}}_\mathbf{i})(\hat{\mathbf{n}} \cdot \hat{\mathbf{k}}_\mathbf{i})\hat{\mathbf{q}}_\mathbf{i}(1 - R^{TE}) \\ &+(\hat{\mathbf{e}}_\mathbf{i} \cdot \hat{\mathbf{p}}_\mathbf{i})(\hat{\mathbf{n}} \times \hat{\mathbf{k}}_\mathbf{i})(1 - R^{TM})\big].\end{aligned} \tag{6}$$

where $\hat{\mathbf{e}}_\mathbf{i}$ is the polarization versor of the incoming wave, R^{TE} and R^{TM} the reflection coefficients at the interface for TE and TM waves, respectively, and η_i the impedance of the medium the wave is propagating in [1].

From there, the total reflected and transmitted fields at some reception point $\mathbf{r_r}$, denoted $\mathbf{E_s}(\mathbf{r_r})$ and $\mathbf{E_t}(\mathbf{r_r})$, respectively, of a surface subdivided into N facets can be shown to be given by [1] :

$$\begin{aligned}\mathbf{E_s}(\mathbf{r_r}) = &ik_i \sum_\alpha \frac{E_i(\mathbf{r}_\alpha)}{4\pi|\mathbf{r_r} - \mathbf{r}_\alpha|}\left[\mathbf{I} - \hat{\mathbf{k}}_\mathbf{s}\hat{\mathbf{k}}_\mathbf{s}\right] \\ &\cdot \left[\eta_i \hat{\mathbf{H}}_\parallel(\mathbf{r}_\alpha) + \hat{\mathbf{k}}_\mathbf{s} \times \hat{\mathbf{E}}_\parallel(\mathbf{r}_\alpha)\right] \Phi_\alpha(\mathbf{r_i}, \mathbf{r_r}),\end{aligned} \tag{7}$$

$$\begin{aligned}\mathbf{E_t}(\mathbf{r_r}) = &-ik_r \sum_\alpha \frac{E_i(\mathbf{r}_\alpha)}{4\pi|\mathbf{r_r} - \mathbf{r}_\alpha|}\left[\mathbf{I} - \hat{\mathbf{k}}_\mathbf{t}\hat{\mathbf{k}}_\mathbf{t}\right] \\ &\cdot \left[\eta_r \hat{\mathbf{H}}_\parallel(\mathbf{r}_\alpha) + \hat{\mathbf{k}}_\mathbf{t} \times \hat{\mathbf{E}}_\parallel(\mathbf{r}_\alpha)\right] \Phi_\alpha(\mathbf{r_i}, \mathbf{r_r}),\end{aligned} \tag{8}$$

where

$$\Phi_\alpha(\mathbf{r_i}, \mathbf{r_r}) = \iint_{\Delta_\alpha} d\Sigma' \left\{e^{i(k_r|\mathbf{r_r} - \mathbf{r}'| + k_i|\mathbf{r}' - \mathbf{r_i}|)}\right\}, \tag{9}$$

is the factor regrouping total phase contribution of the return from the facet Δ_α. In the previous equations, $\mathbf{r}_\alpha$ represents a privileged position in the considered facet, typically its geometrical centre (see *e.g.*, [1][5]), and $E_i(\mathbf{r}_\alpha)$ is the amplitude of the incident field at given point $\mathbf{r}_\alpha$. $\hat{\mathbf{k}}_\mathbf{s}$ is the unit vector pointing in the backscattering direction and $\hat{\mathbf{k}}_\mathbf{t}$ the unit vector pointing in the transmitted direction. For a transmission problem, the incident and the reflected fields do not lie in the same medium, hence the use of k_r and η_r, which are the wavenumber and the impedance in the reception medium, respectively, in equation (8). Note that for monostatic configuration, we have $\mathbf{k_s} = -\mathbf{k_i}$ in the reflection equation (7).

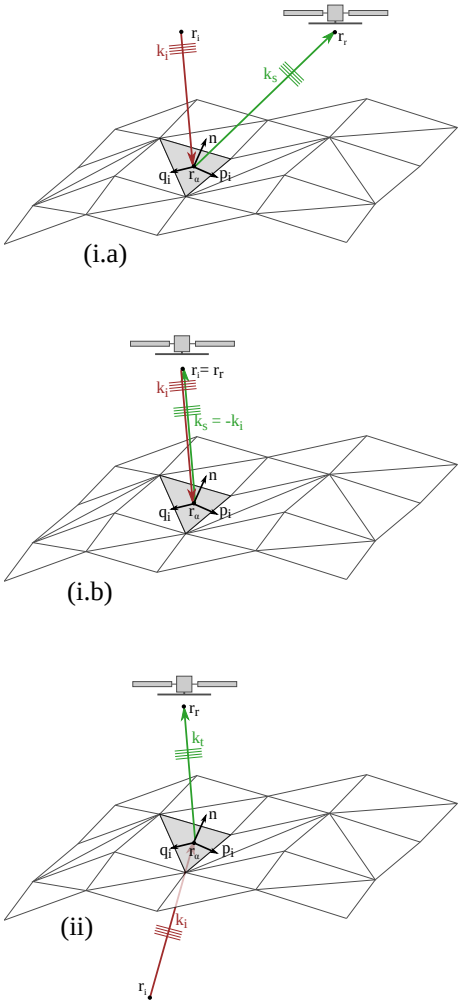

Fig. 1. Illustration of vector quantities used in three possible configurations. (i.a) a bistatic configuration where reflection is analysed, (i.b) a monostatic configuration where reflection is analysed, and (ii) a bistatic configuration where transmission is analysed.

The so-called Stratton-Chu integral is a rewritten version of eqs. (7)-(8) as a volume integral. In this paper we use "Huygens' principle" and "Stratton-Chu integral" interchangeably.

B. Facet phase calculation method

In this section we briefly recall the equations of [1]. Essentially, the main idea behind this work is to perform a Taylor expansion of the argument of the exponential in eq. (9) and compute the integral accordingly. This results in a readily-applicable analytical formula. The exponential is expressed as $e^{i(k_r|\mathbf{r_r} - \mathbf{r}'| + k_i|\mathbf{r}' - \mathbf{r_i}|)} = e^{2i(-a_0 x - b_0 y + d_0)}$, with some parameters a_0, b_0, and d_0 depending on the scattering geometry.

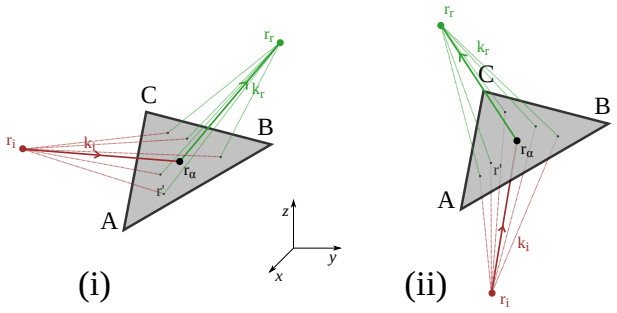

Fig. 2. Graphical representation of the integral given in eq. (9). A, B, and D are the coordinates triangle vertices, while $\mathbf{r}_\alpha$ is the position of the triangle incentre. $\mathbf{r}'$ and the dotted lines represent several examples of paths appearing in the integral in eq. (9). (i) represents a reflection and (ii) a transmission.

The equation proposed in [1] is as follows:

$$\begin{aligned}\Phi_\alpha(\mathbf{r_i},\mathbf{r_r}) =& J\frac{e^{id_0}}{(2i)^2 b_0}\\ &\left[\frac{e^{-2ib_0\beta_1}}{a_0+b_0\alpha_1}\left(e^{-2iD_x(a_0+b_0\alpha_1)}-e^{-2iA_x(a_0+b_0\alpha_1)}\right)\right.\\ &+\frac{e^{-2ib_0\beta_2}}{a_0+b_0\alpha_2}\left(e^{-2iB_x(a_0+b_0\alpha_2)}-e^{-2iD_x(a_0+b_0\alpha_2)}\right)\\ &\left.\frac{e^{-2i(b_0D_y+A_xa_0)}-e^{-2i(b_0D_y+B_xa_0)}}{a_0}\right],\end{aligned} \tag{10}$$

with A, B and C being the the coordinates of the vertices of the triangle considered and D a point in the (AB) segment such that $(CD)\perp(AB)$, $\alpha_1=(A_y-C_y)/(A_x-C_x)$, $\beta_1=C_y-\alpha_1C_x$, $\alpha_2=(B_y-C_y)/(B_x-C_x)$, $\beta_2=C_y-\alpha_2C_x$, and $J=\sqrt{a^2+b^2+1}$, where a, b, and c are the coefficients of the equation of the plane $ax+by+d=z$ characterizing the triangle. a_0, b_0 and d_0 are shown to be:

$$a_0=\frac{1}{2}(k_{i,x}-k_{r,x})+\frac{a}{2}(k_{i,z}-k_{r,z}) \tag{11}$$

$$b_0=\frac{1}{2}(k_{i,y}-k_{r,y})+\frac{b}{2}(k_{i,z}-k_{r,z}) \tag{12}$$

$$d_0=\frac{1}{2}(\mathbf{r_i}\cdot\mathbf{k_i}-\mathbf{r_r}\cdot\mathbf{k_r})+\frac{d}{2}(k_{i,z}-k_{r,z}) \tag{13}$$

where $\mathbf{k_r}$, the wavevector of the received wave, collinear with $\mathbf{r_r}-\mathbf{r}_\alpha$, represents either $\mathbf{k_s}$ or $\mathbf{k_t}$, depending on whether we are using eq. (7) or (8) (as shown in Fig. 2). Please note that these equations have been slightly rewritten in order to facilitate the use of wavenumbers $\mathbf{k_i}$ and $\mathbf{k_r}$ of different norms (in [1], the incident and received waves are implicitly considered to lie in the same medium).

The main interest of the linear phase approximation is that it poses much less stringent constrains on the DEM resolution. Indeed, while constant phase approximation simulations need facets at least as small at $\lambda/10$, linear phase approximation ones requires facets of about $n\sqrt{\lambda h/2}$, where h is the platform altitude and n a constant usually set at 0.2 [1].

C. Stratton-Chu with one subsurface layer

In this section, we recall the principles behind the methods developed by Fa *et al.* [5], and Kobayashi *et al.* [12][13], which both seek to coherently treat problems with a single subsurface layer. In both methods, the surface is treated using a version of the reflection Stratton-Chu integral, shown at eq. (1), where the phase of each echo is computed according to the constant phase approximation ($\Phi_\alpha(\mathbf{r_i},\mathbf{r_r}) = \mathcal{A}(\Delta_\alpha)e^{i(k_r|\mathbf{r_r}-\mathbf{r}'|+k_i|\mathbf{r}'-\mathbf{r_i}|)}$, where $\mathcal{A}(\Delta_\alpha)$ is the area of the facet Δ_α). As previously stated, this choice demands much smaller facets and thus much longer computation times.

In [12][13], the subsurface echoes are treated by computing the electric field at each point of the subsurface using the Stratton-Chu formula. This approach is exact, in the sense that it does not require more approximations than those already set forth by Kirchhoff's approximation. However it is computationally very expensive.

In [5], the subsurface is treated using the classical laws of optics for planar waves impinging planar dielectric interfaces (see *e.g.*, [11][14][30]). These laws are used to compute (i) the transmitted wavevector and field amplitude at the surface, (ii) the reflected wavevector and amplitude at the subsurface, and lastly (iii) the re-transmitted wavevector and field amplitude. The amplitudes are decomposed into TE and TM modes to allow the use of the correct Fresnel coefficient at each interface. At step (iii), the obtained field is fed into Stratton-Chu, yielding the field observed at the antenna. This method does not capture the complete behaviour of the subsurface electromagnetic field (as signals do not propagate as plane waves within it), but was found to produce satisfactory results for realistic sounding scenarios with greatly improved computational efficiency [5][16].

III. Proposed Multilayer Coherent Simulator

In this section we present our proposed multilayer coherent simulator, and in particular, how subsurface echo calculations were treated.

Fig. 3 shows the global architecture of the technique. The fundamental input variables that the simulator considers are a layered digital elevation model (DEM) and a geoelectrical model. They consist of a series of digitized surfaces at various depth ($S_0(x,y)$ for the surface and $S_{m=1..M}(x,y)$ for the subsurface layers) with given dielectric properties in-between those layers. These digitized surfaces are then triangulated, thus obtaining a collection of M sets $\left\{\Delta_\alpha^{m=0..M}\right\}_{\alpha=1,\dots,N}$ containing N triangles each. We consider a spaceborne radar instrument flying over this terrain at a given altitude and speed (which can vary along the azimuth direction). The pulsed nature of a radar sounder (it collects acquisitions with a finite PRF) provides a convenient way to discretize the trajectory of the spacecraft, which is denoted as $\mathbf{x}_{s/c}(j)$ in Fig. 3 (it will be referred to as $(\mathbf{r_r};j)$ in the next section for notational clarity). For each position j of the spacecraft, the simulator will consider all the triangles within a predefined footprint, which is a circle of given radius centred around the vertical projection of $\mathbf{x}_{s/c}(j)$ on the surface, and will compute all the echoes coming from this portion of terrain (surface and subsurface), thus obtaining the complete range line for that position. The simulator computes many of such positions in parallel as they are all independent from each other. At the end,

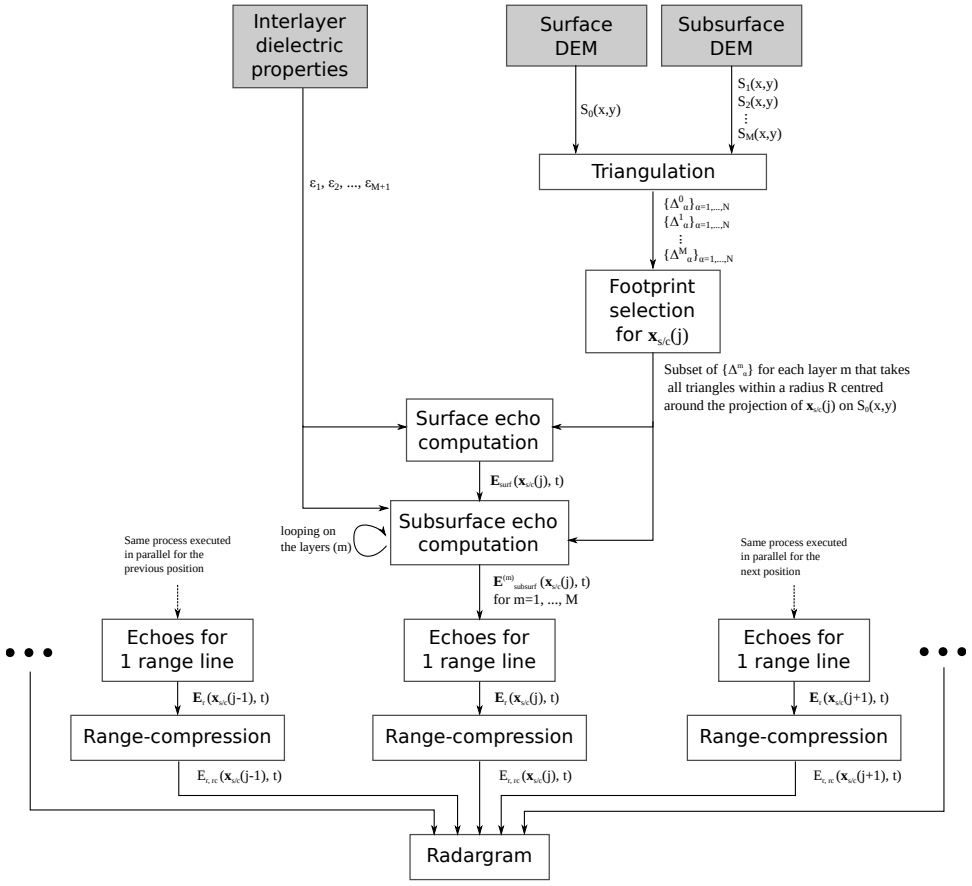

Fig. 3. Block diagram showing the architecture of the proposed simulator.

range-compression is applied to each range line, resulting in a B-scan (or radargram).

To compute the electrical field, the simulator follows an hybrid approach using both geometrical optics and physical optics. Ray-tracing is used to model the incoming signal and the propagation of fields within the subsurface. The incoming wavevectors are modelled with respect to the triangle incentres. On the contrary, the field emitted by a surface facet, which can come either from a direct reflection or from a transmission from a deeper subsurface layer, is computed rigorously using either of the Stratton-Chu integrals given above.

A monopole emitting antenna is considered. At a given position $\mathbf{r}$, the emitted field is thus given by:

$$\mathbf{E_i}(\mathbf{r}) = \frac{E_0}{4\pi|\mathbf{r_i}-\mathbf{r}|} e^{ik_i|\mathbf{r_i}-\mathbf{r}|}\hat{\mathbf{e}}_\mathbf{i} \tag{14}$$

where E_0 is the amplitude of the field emitted at the antenna.

The calculation of the electric field reflected by the surface and the subsurface layers will be explained in subsection A to C, t. As the procedure is the same for every position j of the spacecraft, that index will be dropped for clarity (it will be reintroduced in subsection D when needed).

A. Surface response

Surface echoes are direct reflections and are thus computed using the reflection Stratton-Chu integral where $\hat{\mathbf{e}}_\mathbf{i}$ being the polarization chosen in (14), and $E_i(\mathbf{r}_\alpha)$ being calculated from that same expression. The equation is furthermore specialized to the case of a monostatic configuration, *i.e.*, assuming $\mathbf{r_i} = \mathbf{r_r}$ and $\mathbf{k_r} = \mathbf{k_s} = -\mathbf{k_i}$.

$$\begin{aligned}\mathbf{E}_{\text{surf}}(\mathbf{r_r}) =& ik_i \sum_\alpha \frac{E_0}{(4\pi)^2|\mathbf{r_r}-\mathbf{r}_\alpha|^2}\left[\mathbf{I} - \hat{\mathbf{k_i}}\hat{\mathbf{k_i}}\right] \\ &\cdot \left[\eta_i \hat{\mathbf{H}}_\parallel(\mathbf{r}_\alpha) - \hat{\mathbf{k_i}} \times \hat{\mathbf{E}}_\parallel(\mathbf{r}_\alpha)\right] \Phi_\alpha(\mathbf{r_r}, \mathbf{r_r}),\end{aligned} \tag{15}$$

B. Subsurface response

Layers are denoted with an index (subscript or superscript, depending on readability) in parenthesis, with $m = 1$ representing the surface, $m = 2$ the first subsurface layer, and so on.

a) Transmissions and reflections: Propagation of fields throughout the subsurface is mainly addressed using geometrical optics. Whenever a wave interacts with a layer, the transmitted and reflected wavevectors are computed according to Snell's law (see *e.g.* [11]). The transmitted wavevector is given by :

$$\begin{aligned}\hat{\mathbf{k}}_\mathbf{t}^{(\mathbf{m+1})} =& \frac{n^{(m)}}{n^{(m+1)}}\hat{\mathbf{k}}_\mathbf{t}^{(\mathbf{m})} \\ &+ \left(\frac{n^{(m)}}{n^{(m+1)}}\hat{\mathbf{k}}_\mathbf{t}^{(\mathbf{m})}\cos(\theta_{inc}) - \cos(\theta_{tra})\right)\hat{\mathbf{n}},\end{aligned} \tag{16}$$

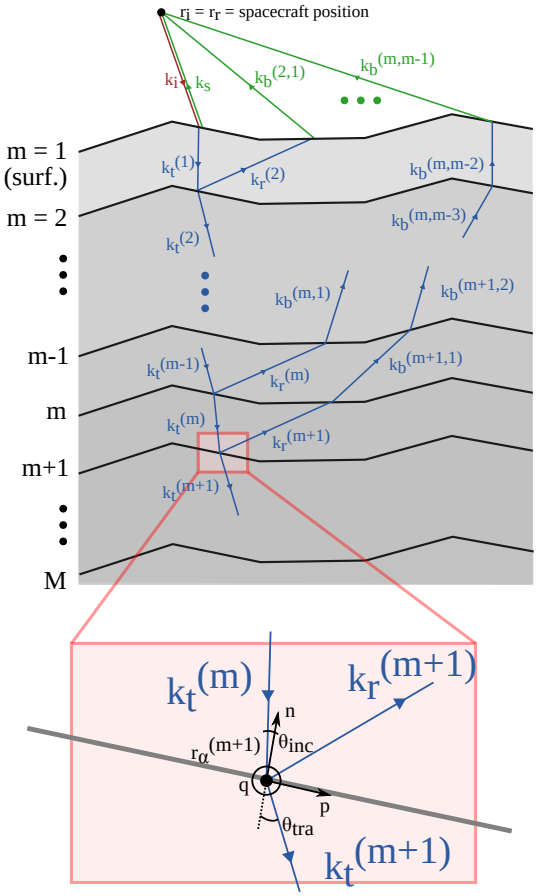

Fig. 4. Graphical representation of transmitted, reflected and backscattered (upwards transmission) wavevectors.

with $\hat{\mathbf{k}}_\mathbf{t}^{(\mathbf{0})}$, the wavevector (of unit norm) of the ray hitting the surface, which is the wavevector of the emitted field *i.e.*,

$$\hat{\mathbf{k}}_\mathbf{t}^{(\mathbf{0})} \equiv \hat{\mathbf{k}}_\mathbf{i}. \tag{17}$$

θ_{inc} and θ_{tra} are the angles of incidence and transmission, respectively, of the ray with respect to the normal $\hat{\mathbf{n}}$. They are computed from $\hat{\mathbf{k}}_\mathbf{t}^{(\mathbf{m})}$ using Snell's law. These quantities refer to the considered interface, and the $(m+1)$ superscript has been dropped to avoid making notations too cumbersome: $\theta_{inc}^{(m+1)} \equiv \theta_{inc}$, $\theta_{tra}^{(m+1)} \equiv \theta_{tra}$, and $\hat{\mathbf{n}}(\mathbf{r}_\alpha^{(m+1)}) \equiv \hat{\mathbf{n}}$, where $\mathbf{r}_\alpha^{(m+1)}$ is the position of the incentre of the triangle hit upon by the ray with wavevector $\hat{\mathbf{k}}_\mathbf{t}^{(\mathbf{m})}$. The reflected wavevector is given by :

$$\hat{\mathbf{k}}_\mathbf{r}^{(\mathbf{m+1})} = \hat{\mathbf{k}}_\mathbf{t}^{(\mathbf{m})} - 2\hat{\mathbf{n}}\left(\hat{\mathbf{n}} \cdot \hat{\mathbf{k}}_\mathbf{t}^{(\mathbf{m})}\right). \tag{18}$$

The intensity of the TE and TM components of the transmitted electrical field are computed according to classical optics (see *e.g.*, [11]):

$$\begin{aligned}\mathbf{E}_\mathbf{t}^{\mathbf{TM},(\mathbf{m+1})} = &\left[\text{att}\left(\mathbf{E}_\mathbf{t}^{\mathbf{TE},(\mathbf{m})} + \mathbf{E}_\mathbf{t}^{\mathbf{TM},(\mathbf{m})}\right)\cdot\hat{\mathbf{p}}\right] \\ &\frac{n^{(m)}}{n^{(m+1)}}\left(1 + R_{(m,m+1)}^{TM}\right)\hat{\mathbf{q}} \times \hat{\mathbf{k}}_\mathbf{t}^{(\mathbf{m+1})},\end{aligned} \tag{19}$$

$$\begin{aligned}\mathbf{E}_\mathbf{t}^{\mathbf{TE},(\mathbf{m+1})} = &\left[\text{att}\left(\mathbf{E}_\mathbf{t}^{\mathbf{TE},(\mathbf{m})} + \mathbf{E}_\mathbf{t}^{\mathbf{TM},(\mathbf{m})}\right)\cdot\hat{\mathbf{q}}\right] \\ &\left(1 + R_{(m,m+1)}^{TE}\right)\hat{\mathbf{q}},\end{aligned} \tag{20}$$

and likewise for the reflected electrical fields :

$$\begin{aligned}\mathbf{E}_\mathbf{r}^{\mathbf{TM},(\mathbf{m+1})} = &\left[\text{att}\left(\mathbf{E}_\mathbf{t}^{\mathbf{TE},(\mathbf{m})} + \mathbf{E}_\mathbf{t}^{\mathbf{TM},(\mathbf{m})}\right)\cdot\hat{\mathbf{p}}\right] \\ &R_{(m,m+1)}^{TM}\hat{\mathbf{q}} \times \hat{\mathbf{k}}_\mathbf{r}^{(\mathbf{m+1})},\end{aligned} \tag{21}$$

$$\begin{aligned}\mathbf{E}_\mathbf{r}^{\mathbf{TE},(\mathbf{m+1})} = &\left[\text{att}\left(\mathbf{E}_\mathbf{t}^{\mathbf{TE},(\mathbf{m})} + \mathbf{E}_\mathbf{t}^{\mathbf{TM},(\mathbf{m})}\right)\cdot\hat{\mathbf{q}}\right] \\ &R_{(m,m+1)}^{TE}\hat{\mathbf{q}},\end{aligned} \tag{22}$$

where $\text{att}(A)$ represents the attenuation function, which, in linear media, is given by an exponential decay :

$$\text{att}(A) = Ae^{-\alpha^{(m)} f_c \left|\mathbf{r}_\alpha^{(\mathbf{m+1})} - \mathbf{r}_\alpha^{(\mathbf{m})}\right|}, \tag{23}$$

where $-\alpha^{(m)}$ is the one-way attenuation constant in the medium below layer m, and f_c the central frequency of the radar. Again, vectors $\hat{\mathbf{p}}$ and $\hat{\mathbf{q}}$ implicitly refer to the triangle where the reflection/transmission occurs: $\left\{\hat{\mathbf{k}}_\mathbf{t}^{(\mathbf{m})}, \hat{\mathbf{p}}(\mathbf{r}_\alpha^{(m+1)}), \hat{\mathbf{q}}(\mathbf{r}_\alpha^{(m+1)})\right\} \equiv \left\{\hat{\mathbf{k}}_\mathbf{t}^{(\mathbf{m})}, \hat{\mathbf{p}}, \hat{\mathbf{q}}\right\}$. The initial field $\mathbf{E}_\mathbf{t}^{(\mathbf{0})}$ is the emitted field at the surface of the facet :

$$\mathbf{E}_\mathbf{t}^{\mathbf{TM},(\mathbf{0})} \equiv \mathbf{E}_\mathbf{i}^{\mathbf{TM}}(\mathbf{r}_\alpha), \quad \mathbf{E}_\mathbf{t}^{\mathbf{TE},(\mathbf{0})} \equiv \mathbf{E}_\mathbf{i}^{\mathbf{TE}}(\mathbf{r}_\alpha). \tag{24}$$

b) Upwards transmission: Every reflected wave will be propagating upwards (double reflections are neglected), in the direction of the radar. This "upwards" propagation is also treated in an iterative way. The upwards-transmitted quantities were denoted by an index b to differentiate them from their downwards-transmitted analogues (which are denoted with an index t). For the initial reflected ray coming from a given layer m, the order of the transmission is indicated with an index l, with $l = 1$ corresponding to the first transmitted field (see Fig. 4).

Equations similar to (16), (19) and (20) are used :

$$\begin{aligned}\hat{\mathbf{k}}_\mathbf{b}^{(\mathbf{m;l+1})} = &\frac{n^{(m-l-1)}}{n^{(m-l-2)}}\hat{\mathbf{k}}_\mathbf{b}^{(\mathbf{m;l})} \\ &+ \left(\frac{n^{(m-l-2)}}{n^{(m-l-1)}}\hat{\mathbf{k}}_\mathbf{b}^{(\mathbf{m;l})}\cos(\theta_{inc}) - \cos(\theta_{tra})\right)\hat{\mathbf{n}},\end{aligned} \tag{25}$$

with

$$\hat{\mathbf{k}}_\mathbf{b}^{(\mathbf{m;0})} \equiv \hat{\mathbf{k}}_\mathbf{r}^{(\mathbf{m})}. \tag{26}$$

Regarding the fields, we can write:

$$\begin{aligned}\mathbf{E}_\mathbf{b}^{\mathbf{TM},(\mathbf{m;l+1})} = &\left[\text{att}\left(\mathbf{E}_\mathbf{b}^{\mathbf{TE},(\mathbf{m;l})} + \mathbf{E}_\mathbf{b}^{\mathbf{TM},(\mathbf{m;l})}\right)\cdot\hat{\mathbf{p}}\right]\frac{n^{(m-l-2)}}{n^{(m-l-1)}} \\ &\left(1 + R_{(m-l-1,m-l-2)}^{TM}\right)\hat{\mathbf{q}} \times \hat{\mathbf{k}}_\mathbf{b}^{(\mathbf{m;l+1})},\end{aligned} \tag{27}$$

$$\begin{aligned}\mathbf{E}_\mathbf{b}^{\mathbf{TE},(\mathbf{m;l+1})} = &\left[\text{att}\left(\mathbf{E}_\mathbf{b}^{\mathbf{TE},(\mathbf{m;l})} + \mathbf{E}_\mathbf{b}^{\mathbf{TM},(\mathbf{m;l})}\right)\cdot\hat{\mathbf{q}}\right] \\ &\left(1 + R_{(m-l-1,m-l-2)}^{TE}\right)\hat{\mathbf{q}},\end{aligned} \tag{28}$$

with

$$\mathbf{E_b^{TM,(m;0)}} \equiv \mathbf{E_r^{TM,(m)}}, \quad \mathbf{E_b^{TE,(m;0)}} \equiv \mathbf{E_r^{TE,(m)}}.$$

c) Total subsurface field: Once the fields and the wavevectors have been computed all the way back to the surface, the total field at the antenna is computed using the transmission Stratton-Chu integral in the following configuration. Here, the emitter is not the radar as for the surface case, but rather the incentre of the triangle from which $\mathbf{k_b^{(m;m-2)}}$ has been emitted. In other words, the subsurface is now the source of fields and is radiating through the surface towards the spacecraft. Thus, for the echoes arising from a given layer (m), the transmission Stratton-Chu equation is used with the following quantities:

$$\mathbf{E_i}(\mathbf{r}_\alpha) \equiv \mathbf{E_b^{TM,(m;m-2)}} + \mathbf{E_b^{TE,(m;m-2)}}, \tag{29}$$

$$\hat{\mathbf{k}}_\mathbf{i} \equiv \hat{\mathbf{k}}_\mathbf{b}^{(\mathbf{m};\mathbf{m-2})}, \tag{30}$$

$$\mathbf{r_i} \equiv \mathbf{r}_{\boldsymbol{\alpha}}^{(\mathbf{m};\mathbf{m-2})}. \tag{31}$$

Thus, the total electric field emitted by subsurface layer (m) received at the spacecraft is given by:

$$\begin{aligned}\mathbf{E}_{\text{subsurf}}^{(m)}(\mathbf{r_r}) = &- ik_i \sum_\alpha \frac{E_b^{(m;m-2)}}{4\pi \left|\mathbf{r_r} - \mathbf{r}_{\boldsymbol{\alpha}}^{(\mathbf{m};\mathbf{m-1})}\right|} \left[\mathbf{I} - \hat{\mathbf{k}}_\mathbf{t}\hat{\mathbf{k}}_\mathbf{t}\right] \\ &\cdot \left[\eta_i \hat{\mathbf{H}}_\parallel \left(\mathbf{r}_{\boldsymbol{\alpha}}^{(\mathbf{m};\mathbf{m-1})}\right) + \hat{\mathbf{k}_\mathbf{t}} \times \hat{\mathbf{E}}_\parallel \left(\mathbf{r}_{\boldsymbol{\alpha}}^{(\mathbf{m};\mathbf{m-1})}\right)\right] \\ &\Phi_{\text{subsurf}}^{(m)},\end{aligned} \tag{32}$$

where $\hat{\mathbf{k}_\mathbf{b}}^{(\mathbf{m};\mathbf{m-1})} \equiv \hat{\mathbf{k}_\mathbf{t}}$ is the versor pointing in the backscattering direction. The polarisation vector $\mathbf{e_i}$ is now that of $\mathbf{E_b^{(m;m-2)}} = \mathbf{E_b^{TM,(m;m-2)}} + \mathbf{E_b^{TE,(m;m-2)}}$, while the $\hat{\mathbf{n}}$, $\hat{\mathbf{q}}_\mathbf{i}$ and $\hat{\mathbf{p}}_\mathbf{i}$ versors refer to the $\Delta_\alpha^{(m;m-1)}$ surface triangle hit upon by the ray defined by $\mathbf{k_b^{(m;m-2)}}$. [Note that, by virtue of eq. (24), $E_b^{(m;m-2)}$ already contains in it the $(4\pi\,|\mathbf{r_i} - \mathbf{r}_\alpha|)^{-1}$ spherical spreading factor of the emitted field. Hence only a $(4\pi|\mathbf{r_r} - \mathbf{r}_{\boldsymbol{\alpha}}^{(\mathbf{m};\mathbf{m-1})}|)^{-1}$ factor for the propagation from the surface to the spacecraft is needed in eq. (32).]

The phase of the received signal is given by:

$$\begin{aligned}\Phi_{\text{subsurf}}^{(m)} = \Phi\left(\mathbf{r}_{\boldsymbol{\alpha}}^{(\mathbf{m};\mathbf{m-2})}, \mathbf{r_r}\right) &\left[\prod_{j=1}^{m-1} e^{-ik_i n_j \left|\mathbf{r}_{\boldsymbol{\alpha}}^{(\mathbf{j+1})} - \mathbf{r}_{\boldsymbol{\alpha}}^{(\mathbf{j})}\right|}\right] \\ \cdot \left[e^{-ik_i n_{m-1}\left|\mathbf{r}_{\boldsymbol{\alpha}}^{(m)} - \mathbf{r}_{\boldsymbol{\alpha}}^{(m;1)}\right|} \prod_{j=1}^{m-2} e^{-ik_i n_{m-j}\left|\mathbf{r}_{\boldsymbol{\alpha}}^{(\mathbf{m;j+1})} - \mathbf{r}_{\boldsymbol{\alpha}}^{(\mathbf{m;j})}\right|}\right]&.\end{aligned} \tag{33}$$

The first factor is the phase contribution of the surface facet (calculated as if the field was emitted at the incentre of the previous triangle) for correct interference reconstruction, the second accounts for the phase accumulated by the field in all "downwards" transmissions, and the third, in the "upwards" transmissions up to $\Delta_\alpha^{(m;m-2)}$.

The transmission Stratton-Chu integral is thus only computed at the surface, taking as input the field coming from the subsurface layer (along with its full propagation history within the subsurface), instead of computing it at each boundary, as it was done in [12] for a single subsurface layer. While in theory this leads to miss a part of the electromagnetic response (as in [5]), the echoes computed with this formula are satisfactory for all practical purposes, as we will demonstrated in sections IV and V. It is thus a reasonable compromise between accuracy and computational efficiency.

C. Time dependence

All the electric fields described in the previous sections showed no time-dependence. In this section, the time-dependence of those fields is introduced along with the reasons that made such a decoupling possible.

The emitted signal is taken to be a Hann-windowed chirp:

$$s(t) = W(t) \exp\left[i\pi \frac{B}{T}(t - T/2)^2\right] \tag{34}$$

where B is the radar bandwidth, T the pulse length, and $W(t)$ is the windowing function, which is zero for $t < 0$ and $t > T$. The time-dependent emitted field at the emission point is thus given by $\mathbf{E_i}(\mathbf{r_i}, t) = \mathbf{E_i}(\mathbf{r_i})s(t)$. The time-evolution of the field received from a given point or facet $\mathbf{E_r}(\mathbf{r_r}, t)$ is given by $\mathbf{E_r}(\mathbf{r_r}, t) = \mathbf{E_r}(\mathbf{r_r})s(t - \tau)$, where τ represents the delay with which the reflected signal arrives back at the antenna. Such a decoupling is only possible if the bandwidths of the signals involved are small. Indeed, the rigorous way to use the Stratton-Chu integral on such signals would be to decompose them into their Fourier components (which are plane waves) and to compute how each of these components is reflected. However, due to the narrow bandwidths generally used in radar sounders and taking into account the precision required by the use of simulations, we make the approximation of considering the central frequency of the radar only. Accordingly, (15) and (32) can be written as

$$\begin{aligned}\mathbf{E}_{\text{surf}}(\mathbf{r_r}, t) = &ik_i \sum_\alpha \frac{E_0 s(t - \tau)}{(4\pi)^2 |\mathbf{r_r} - \mathbf{r}_\alpha|^2} \left[\mathbf{I} - \hat{\mathbf{k}_\mathbf{i}}\hat{\mathbf{k}_\mathbf{i}}\right] \\ &\cdot \left[\eta_i \hat{\mathbf{H}}_\parallel(\mathbf{r}_\alpha) - \hat{\mathbf{k}_\mathbf{i}} \times \hat{\mathbf{E}}_\parallel(\mathbf{r}_\alpha)\right] \Phi_\alpha(\mathbf{r_r}, \mathbf{r_r}),\end{aligned} \tag{35}$$

$$\begin{aligned}\mathbf{E}_{\text{subsurf}}^{(m)}(\mathbf{r_r}, t) = &- ik_i \sum_\alpha \frac{E_b^{(m;m-2)} s(t - \tau)}{4\pi \left|\mathbf{r_r} - \mathbf{r}_{\boldsymbol{\alpha}}^{(\mathbf{m};\mathbf{m-1})}\right|} \left[\mathbf{I} - \hat{\mathbf{k}}_\mathbf{t}\hat{\mathbf{k}}_\mathbf{t}\right] \\ &\cdot \left[\eta_i \hat{\mathbf{H}}_\parallel \left(\mathbf{r}_{\boldsymbol{\alpha}}^{(\mathbf{m};\mathbf{m-1})}\right) + \hat{\mathbf{k}_\mathbf{t}} \times \hat{\mathbf{E}}_\parallel \left(\mathbf{r}_{\boldsymbol{\alpha}}^{(\mathbf{m};\mathbf{m-1})}\right)\right] \\ &\Phi_{\text{subsurf}}^{(m)},\end{aligned} \tag{36}$$

where the delay τ is in each case a quantity depending on α, the index of the considered facet. For a surface echo, this delay is simply the two-way signal travel time in vacuum $\tau = 2|\mathbf{r_r} - \mathbf{r_\alpha}|/c$. For an echo coming from the subsurface layer (m), this delay is given by

$$\begin{aligned}\tau = \frac{1}{c} &\left[|\mathbf{r_i} - \mathbf{r_\alpha}| + \left|\mathbf{r_i} - \mathbf{r}_{\boldsymbol{\alpha}}^{(\mathbf{m};\mathbf{m-1})}\right| + \sum_{i=1}^{m-1} \left|\mathbf{r}_{\boldsymbol{\alpha}}^{(\mathbf{i})} - \mathbf{r}_{\boldsymbol{\alpha}}^{(\mathbf{i+1})}\right| \right. \\ &\left. + \left|\mathbf{r}_{\boldsymbol{\alpha}}^{(\mathbf{m})} - \mathbf{r}_{\boldsymbol{\alpha}}^{(\mathbf{m};1)}\right| + \sum_{i=1}^{m-2} \left|\mathbf{r}_{\boldsymbol{\alpha}}^{(\mathbf{m;i})} - \mathbf{r}_{\boldsymbol{\alpha}}^{(\mathbf{m;i+1})}\right|\right].\end{aligned} \tag{37}$$

Note that this way of calculating delays confounds the incentre of the hit-upon triangle with the actual impact point of the incoming ray, and is therefore an approximation with regard to reality. That, however, is acceptable. Indeed, this assumption is equivalent to introducing an imprecision on the position of the subsurface refractors which leads to, at most, a random error of a few percent on the optical path of the considered ray. Thus, for all practical purposes, this approximation has no impact on the backscattered echoes. This assertion is supported by the satisfying results obtained in sections IV and V.

D. Post-processing

At detection, the range line signal $E_{r,rc}(\mathbf{r_r}, t)$ is obtained by multiplying the received electric field by the antenna gain and polarization $\mathbf{A}$, $E_r(\mathbf{r_r}, t) = \mathbf{A} \cdot \mathbf{E_r}(\mathbf{r_r}, t)$, and cross-correlating it with the input signal $s(t)$ in order to reveal the observed features: $E_{r,rc}(\mathbf{r_r}, t) = \int_{-\infty}^{\infty} E_r(\mathbf{r_r}, t + t')s(t')\mathrm{d}t'$ (range compression). With the use of a chirp as transmitting signal, the result after convolution will resemble a cardinal sinus. A carefully-chosen windowing function is generally applied to attenuate the sidelobes of this function, at the price of widening the main lobe and thus reducing the range resolution.

Given $E_{r,rc}(\mathbf{r_r}, t; j)$ at each position j of the radar, it is possible to simulate the complete radargram of the observation track. In particular, the usual power radargram in deciblels can be obtained by computing $10 \log_{10} |E_{r,rc}(\mathbf{r_r}, t)|^2$. From there, other processing algorithms developed for treating radar data can be applied (*e.g.*, focusing, feature detection). However, they are outside the scope of this paper, as we focus our attention on the electromagnetic modelling.

IV. Analysis of the Simulation Accuracy and Reliability

In this section, we investigate the behaviour of the simulator with respect to all its main parameters: facet size, frequency, bandwidth, terrain roughness, layer depth and dielectric constant. A four-layer rough procedurally-generated DEM was used to this purpose.

Unless otherwise mentioned, the four-layer test terrain is the one shown on Fig. (5). The surface is generated through fractional Brownian motion (fBm) process with $H = 0.7$ and is characterised by an RMS height of 39 m. The three subsurface layers are copies of the surface placed at depths $d_1 = 150$ m, $d_2 = 300$ m, $d_3 = 450$ m. The dielectric constants are $\epsilon_1 = 4 + i0.004$, $\epsilon_2 = 6 + i0.0006$, $\epsilon_3 = 5 + i0.05$, and $\epsilon_4 = 8$. The instrument considered for the simulations has a central frequency of $f = 10$ MHz and a bandwidth of $B = 5$ MHz (unless otherwise mentioned), hovers at an altitude of 100 km, and a power of 800 W. The radius of the first Fresnel zone is $R_{1F} = 1225$ m. The transmitted signal is a 100 μs-long Hann-windowed chirp sampled at $10B$. The rangelines shown throughout this section are obtained by averaging 20 acquisitions over the same track, with the distance between those acquisitions is set to 150 m.

The footprint of the simulations is set to $R = 15$ km, thus simulating clutter competing with subsurface features up to an apparent depth of $\sqrt{h^2 + R^2} - h = 1200$m.

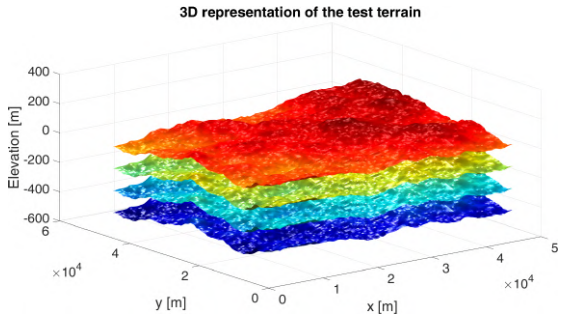

Fig. 5. Three-dimensional representation of the base DEM used in the reliability analysis (axes are not to scale).

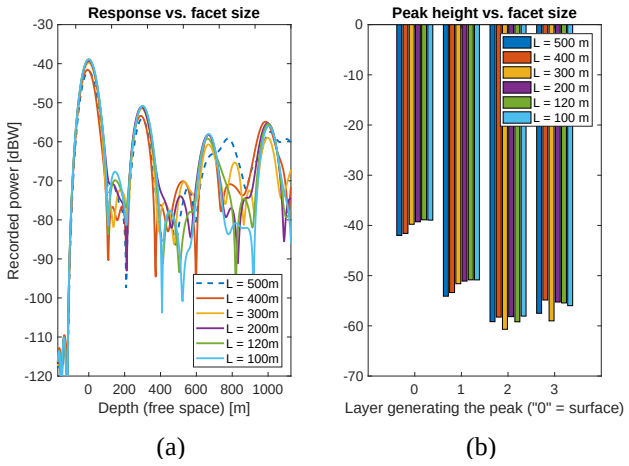

Fig. 6. Simulated range lines obtained with different facet sizes. (a) Comparison between the obtained range lines. (b) Comparison between the peak power of each layer (taken from the (a) graph). DEM shown in Fig. 5.

A. Facet size

Five values for the facet length L were tested: $L = 100$, 120, 200, 300, 400, and 500 m. The DEM was reinterpolated in order to conserve the physical dimensions of the scene. Fig. 6 compares the average range-line obtained in each case, and the peak power coming from each layer. One can see that, despite the changes induced by the DEM reinterpolation, the range-lines and the corresponding peak heights are highly consistent up to $L = 500$ m. Beyond that, divergences start to appear in the deeper layers. However $L = 500$ m is a considerable value, being about 40% of the first Fresnel zone radius R_{1F}; it is thus unsurprising that the method loses accuracy in the deeper layers of this rough terrain. Berquin suggested that the optimal value for the linear phase approximation, when used for the surface only, is $L \approx 0.2R_{1F}$ [1]. With a moderate amount of roughness and topography, the present analysis finds this number acceptable. However, since subsurface layers are naturally more sensitive to phase inaccuracies, we observe a more rapid breakdown of the method at higher values of L. To safely assume that the proposed algorithm will produce accurate results in almost all situations, we suggest a value of $L \approx 0.15R_{1F}$.

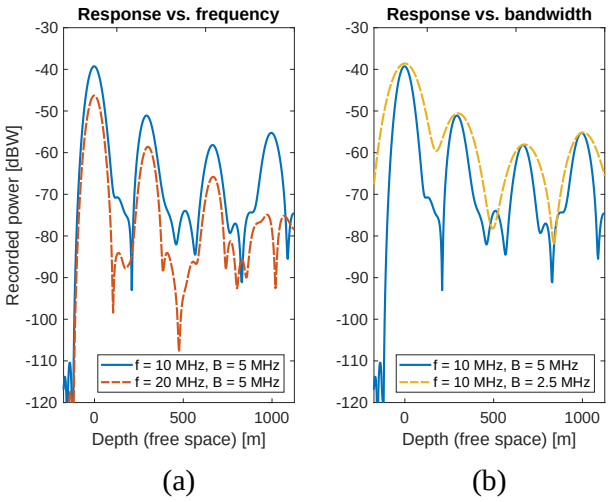

Fig. 7. Simulated range lines obtained with different frequencies and bandwidth. (a) Comparison between $f = 10$ MHz and $f = 20$ MHz, for a fixed bandwidth of 5 MHz. (b) Comparison between $B = 5$ MHz and $B = 2.5$ MHz, for a fixed central frequency of 10 MHz. DEM shown in Fig. 5.

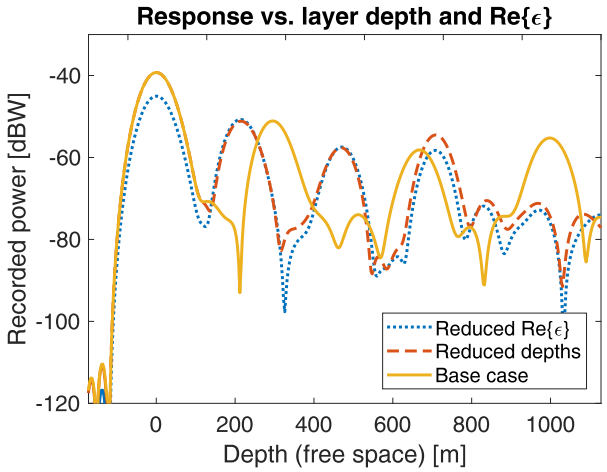

Fig. 8. Simulated range lines obtained with different interlayer dielectric constants, $\epsilon_1 = 2+i0.004$, $\epsilon_2 = 3+i0.0006$, $\epsilon_3 = 2.5+i0.05$, and $\epsilon_4 = 4$, (dotted curve), and with different layer depths, $d_1 = 106$ m, $d_2 = 212$ m, $d_3 = 318$, (dashed curve), along with the base case (solid curve). DEM shown in Fig. 5, with adapted depths in the case of the red curve.

B. Frequency and bandwidth

Three simulations with varying central frequency and chirp bandwidth were performed: the base configuration ($f = 10$ MHz, $B = 5$ MHz), one with doubled frequency ($f = 20$ MHz, $B = 5$ MHz), and one with halved bandwidth ($f = 10$ MHz, B =2.5 MHz). Results are shown on Fig. 7, where one can see that the simulator performs as expected in all cases. When the frequency increases, we observe an overall decrease in the received power due to the smaller antenna effective area. As the signal is more affected by dielectric attenuation, subsurface peaks are also less prominent. This is particularly visible for the fourth layer, which disappears into the background. When the bandwidth decreases, a decrease in the range-resolution can be observed, which, for the main peaks, translates into a broadening of the corresponding central lobes.

C. Dielectric properties and depth of layers

Three simulations with varying interlayer dielectric properties and varying depths were carried out: a base case with the parameters laid out at the beginning of this section, one with reduced dielectric constants, $\epsilon_1 = 2+i0.004$, $\epsilon_2 = 3+i0.0006$, $\epsilon_3 = 2.5+i0.05$, and $\epsilon_4 = 4$, and one with depths reduced by a factor $\sqrt{2}$ ($d_1 = 106$ m, $d_2 = 212$ m, $d_3 = 318$). Fig. 8 shows the obtained result. The simulator performed as expected: both the test cases show peaks at identical reduced depths. The "reduced depths" curve shows power levels similar to the base case, while some peaks of the "reduced $\mathrm{Re}\{\epsilon\}$" curve show a diminished intensity due to the reduction in dielectric contrast. While dielectric attenuation is present in the description of the target areas, the depths of the layers are too small for it to have a significant visible effect.

D. Surface and subsurface roughness

In [12], the authors probe the behaviour of nadir and off-nadir echoes with various amounts of roughness on either the surface or the single subsurface layer. They found that, for layers obeying Gaussian distributions of heights, nadir power tends to remain invariant, whereas off-nadir power increases dramatically with roughness. In our experiment we aim at reproducing this behaviour with our algorithm and to see whether it extends to additional subsurface layers.

The simulations were performed with settings similar to those of the previous sections, except for the DEM. While the number of layers was left unchanged at four, a surface with a Gaussian distribution of height was used, instead of the one generated through a fBm process. The facet size of this DEM was taken to be $L = 200$ m. Since the purpose of this test is to investigate the relative power of clutter and off-nadir echoes, we did not perform a coherent sum of the 20 simulated acquisitions (since this would increase the SNR of the subsurface echoes), but rather display them all separately.

Fig. 9-(a,b,c,d) shows simulations results for four different surface roughness levels modelled with RMS height values of $\sigma_0 = 0.13$, 0.64, 1.3, and 6.4 m, respectively. All subsurface layers are perfectly smooth. It can be seen that the nadir power remains in overall constant, whereas off-nadir power rises rather rapidly by increasing roughness, and masks all subsurface echoes at $\boldsymbol{\sigma_0 = 6.4}$ m. Those findings are consistent with [12].

Fig. 10 shows the impact of subsurface roughness on the simulations. In Fig. 10-(a,c,e), only one subsurface layer is rough, the first, second, and third, respectively, whereas all the others are kept smooth. The rough layer i has a moderate RMS height given by $\sigma_i = 1.3$ m. The effect of roughness on the subsurface response is very similar to what we observed in the surface case: the nadir power values of all layers remain broadly unchanged, whereas off-nadir echoes from a depth equal to the depth of the rough layer increase their intensities. In Fig. 10-(b,d,f), similar settings are investigated, but with a rough surface characterized by a RMS height $\sigma_0 = 1.3$ m. Similar conclusions can be drawn regarding the nadir power.

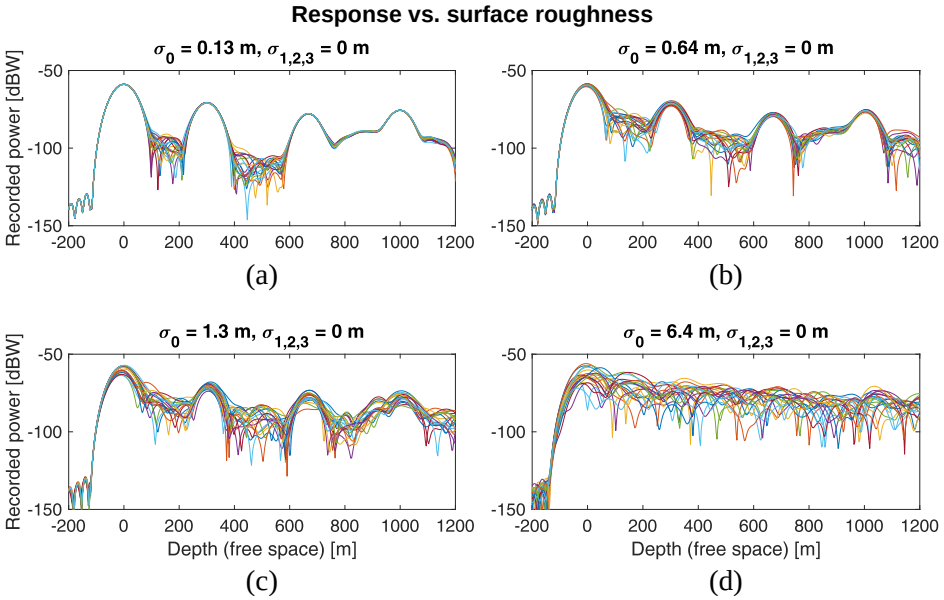

Fig. 9. Simulated range lines obtained with a random Gaussian surface with RMS height (a) $\sigma_0 = 0.13$ m, (b) 0.64 m, (c) 1.3 m, and (d) 6.4 m. Layers are index as "0" = surface, "1" = first subsurface layer, "2" = second subsurface layer, "3" = third and deepest subsurface layer. All subsurface layers are smooth ($\sigma_i = 0,\ i = 1, 2, 3$). Each plot displays the twenty range lines acquired over the track, with no averaging, in order to better highlight the effect of roughness.

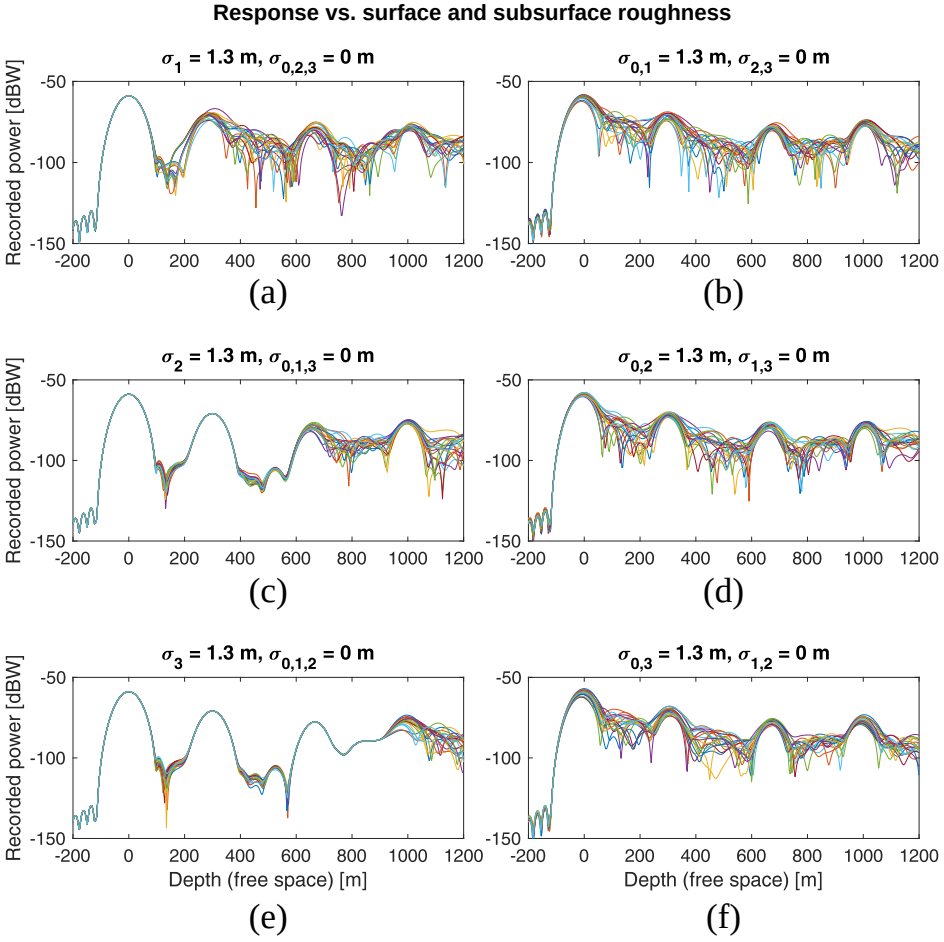

Fig. 10. Simulated range lines obtained with various layers presenting a Gaussian height distribution with RMS height $\sigma_0 = 1.3$ m to various layers : (a) rough first layer, (b) rough surface and rough first layer, (c) rough second layer, (d) rough surface and rough second layer, (e) rough third layer, (f) rough surface and rough third layer. Layers are index as "0" = surface, "1" = first subsurface layer, "2" = second subsurface layer, "3" = third and deepest subsurface layer. Each plot displays the twenty range lines acquired over the track, with no averaging, in order to better highlight the effect of roughness.

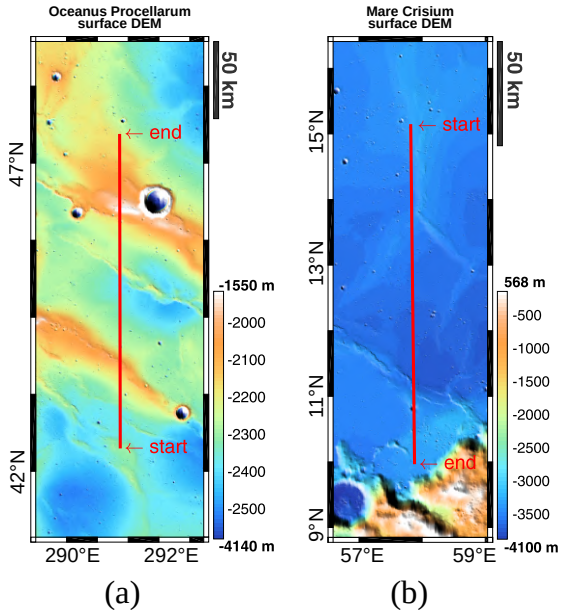

Fig. 11. (a) Ground track the Kaguya probe during acquisition of LRS radargram 20080604124958 (red line) superimposed on a shaded relief map of the surface, an area in Oceanus Procellarum, Moon. (b) Similar image for LRS radargram 20071227143959 of area in Mare Crisium, Moon. "start" and "end" labels refer to the beginning and end of the simulated radargram.

Regarding off-nadir power, one can observe that the effects of the roughness of the surface and that of the considered subsurface layer do not "add up": we obtain a very similar response no matter which subsurface layer is set to be rough. In all cases, we observe that the peak power reflected by each subsurface layer is independent from the roughness of any layer. Thus we can extend the findings of [12] regarding one subsurface layer to multilayer DEMs.

V. Experimental results

We validated the proposed method by selecting radargrams from existing planetary radar sounders and attempting to reproduce them using our simulator. To this end, we used DEMs of the corresponding ground tracks as input to the simulation of the surface, and both the DEM and information inferred from the literature on the investigated area for defining the structure and the position of the subsurface layers. The last part is the most critical as it requires assumptions on the subsurface structure. However, with the support of the literature, it was possible to define realistic scenarios in terms of geoelectrical models to give as input to the simulator.

Due to the intrinsically hypothetical nature of the subsurface DEMs, validation methods involving image substraction and/or coregistration are not appropriate. Thus, the validation was carried out by both a qualitative comparison of the radargrams and a detailed analysis of the statistical properties of the echoes obtained from each layer.

A. Data set 1: Lunar Radar Sounder (LRS)

The simulator was first tested against two radargrams acquired by the Lunar Radar Sounder (LRS) instrument of JAXA's Kaguya lunar probe. The instrument has a central frequency of 5 MHz and a bandwidth of 2 MHz, which corresponds to a free-space range-resolution of 75 metres. The altitude of the spacecraft remains almost constant at about 100 km above the surface. The denomination of the dataset chosen for this study is "Selene Moon LRS 5 Sounder Subsurface High Resolution V2.0". Those are B-scans characterized by a a sampling rate of 6.25 MHz, and a PRF of 20 Hz. No SAR processing or multilooking is applied to generate this data product. The echo power is indicated in dBW/m^2. To make dimensionally meaningful comparisons with our simulation results, we converted the experimental values into dBW by multiplying them by the effective area of a dipole antenna: $P_{\mathrm{RX}}[\mathrm{dBW}] = P[\mathrm{dBW/m^2}]A_{\mathrm{eff}}[\mathrm{m^2}]$, with $A_{\mathrm{eff}} = 1.67\lambda^2/(4\pi)$.

1) Oceanus Procellarum: We present the results obtained by simulating the LRS radargram 20080604124958, a radargram from Oceanus Procellarum, Moon, where a layered subsurface has been discovered [19]. To conduct the simulation, the radar parameters were taken from those of the actual LRS instrument [18]. The surface layer of the multilayer DEM (which has a resolution of 118.5 m) was constructed from measurements by the Lunar Orbiter Laser Atlimeter (LOLA), an altimetry experiment onboard NASA's Lunar Reconnaissance orbiter (LRO) [24]. The two subsurface layers were constructed by placing copies of the surface DEM at the depths indicated in [19]. This is certainly a simplistic way of reproducing the subsurface, but we preferred this option to the construction of a complicated DEM in order to ease off interpretation of the simulation results. The interlayer dielectric properties are those provided in [19] ($\epsilon_1 = 4, \tan\delta_1 = 0.01$, $\epsilon_2 = 6.97, \tan\delta_2 = 0.005$, $\epsilon_3 = 9.33$).

The footprint for this simulation was taken to be a circle with $r = 35$ km. For a (constant) spacecraft altitude of $h = 100$ km, such a footprint will include all the clutter competing with features at an apparent depth $d = \sqrt{\epsilon}(\sqrt{h^2 + r^2} - h) \simeq 6$ km, which is more than enough to capture a comprehensive image of how the subsurface layers, all within the first kilometre, would appear. This amounts to about 651 603 triangles per layer for each range line. Fig. (11-a) shows the trajectory of the spacecraft superimposed on the DEM of the surface.

The simulated radargram is shown in Fig. (12-a). The aspect of the surface and the subsurface do match those of the original radargram, including for the main sources of clutter. Layers are labelled as S0 (surface), S1 (first subsurface layer) and S2 (second subsurface layer).

Fig. (13-a) shows an azimuth-direction averaged range-line for both the simulated radargram and for the original data. From there, the average power of each geological layer can be computed[1]. Table I compares the absolute average power of the surface (S0) and the relative power levels of the subsurface layers with respect to the surface (S1/S0 and S2/S0). One can see that the absolute surface power of the simulated data is only 4.2 dBs higher than that in the original data. More importantly, the relative power levels of the geological layers with respect to the surface closely match those of the original

[1]We recomputed the averages for the LRS data instead of reusing the values of [19]. The values we obtain through our analysis are in any case very close to those reported in [19].

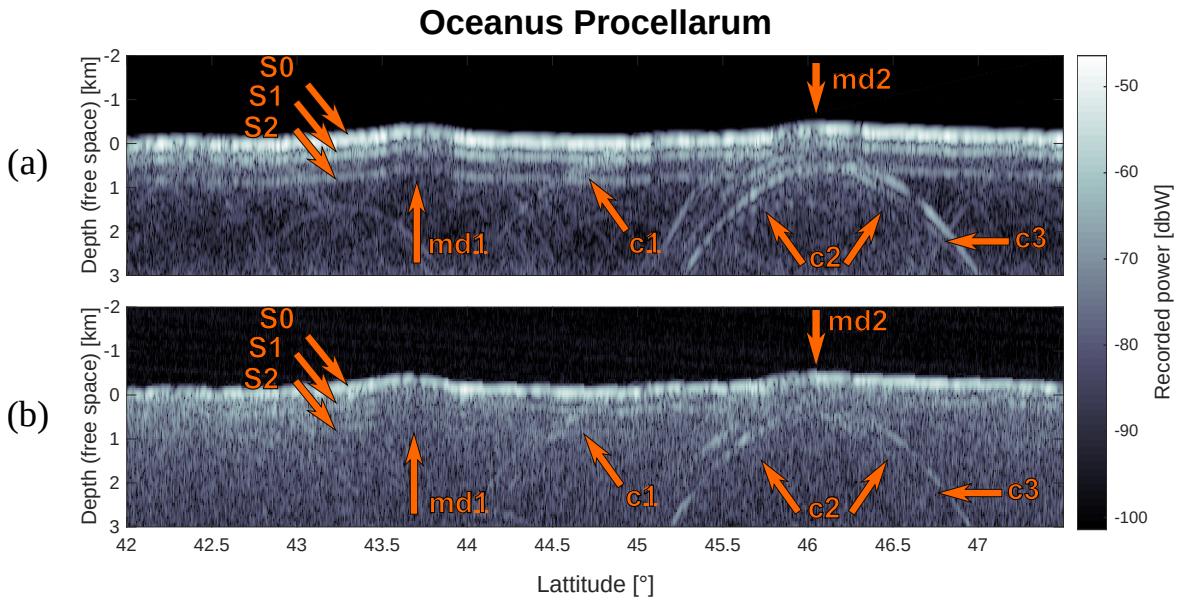

Fig. 12. Comparison between (a) simulation result and (b) LRS radargram 20080604124958 of Oceanus Procellarum. Features of interest are labelled with arrows and are discussed in the text. "S0", "S1", and "S2" are the echoes from the surface, the first subsurface layer, and the second subsurface layer, respectively. "c1", "c2", "c3" are noteworthy clutter sources. "md1" and "md2" are noteworthy geological features.

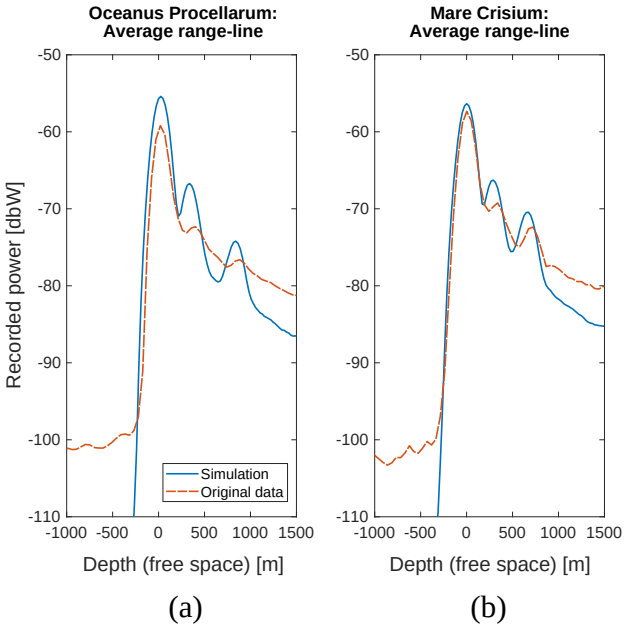

Fig. 13. Azimuth-direction average range-line of the simulated and actual radargrams for (a) LRS radargram 20080604124958 (Oceanus Procellarum), and (b) LRS radargram 20071227143959 (Mare Crisium).

data, being no more than 2 dBs apart. The averaged range-line information highlights an important difference between the simulation and the real radargram, which is the lack of a diffuse response making the subsurface peaks much less prominent. Indeed, the original data show a slow decay with depth whereas the simulated data show a much steeper decrease. We believe the reason behind this difference is that the simulator considers DEMs with relatively large planar facets, devoid of any small-scale roughness, and thus cannot fully reproduce this small-scale diffuse behaviour. The smallest scale of considered features is indeed the resolution of the DEM, *i.e.*, 118.5 m in our case. This diffuse scattering effect could be accounted for by considering rough DEM facets instead of planar ones, for instance by assuming a statistical distribution of heights within each facet. In the simplest case of a Gaussian distribution, this would lead to the a decrease in intensity of the coherent scattering contribution and the apparition of a isotropic incoherent scattering contribution (see *e.g.*, [22][27]). This lack of small-scale roughness in the DEM might also explain the higher absolute power levels obtained with respect to the data from LRS. Additionally, no thermal noise has yet been considered in the simulations.

The simulator correctly reproduces the small drops in surface and subsurface power beneath the mounds at Lat $\simeq$ 43.75°N and Lat $\simeq$ 46°N, labelled "md1" and "md2" in Fig. (12), respectively. It also identifies the main sources of clutter in the original data, labelled "c1", "c2" and "c3", albeit more strongly than in the original image. One can indeed notice a lower amount of clutter and a higher diffuse response in the LRS radargram, for the reasons we explained earlier. The last layer in the simulated radargram is also more visible than in the original data. This difference is probably due to the fact that the actual subsurface is not simply a copy of the surface at a certain depth, but is likely to show some variations in depth, roughness and/or dielectric properties. This highlights the potential use of the simulator as a way to test hypotheses about the subsurface of the targeted area.

Further statistical analysis has been performed. Fig. 14 displays the power histogram of the simulation and the real data for each of the three layers, while table II regroups the properties of these distributions. Four statistical moments were computed: the mean μ, the variance σ, the skewness γ_3, and the kurtosis γ_4. A very good agreement can be observed for all

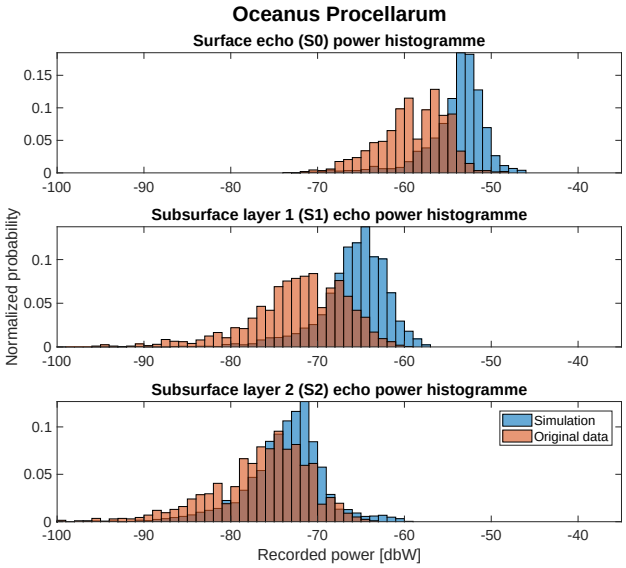

Fig. 14. Oceanus Procellarum radagram: echo brightness histograms for all three layers. The range bin analysed in each case is the one of the corresponding peak in Fig. (13-a).

TABLE I
OCEANUS PROCELLARUM: AVERAGE POWER LEVELS OF THE RECORDED LAYERS

	S0	S1-S0	S2-S0
LRS	-59.2 dBW	-13.1 dBW	-17.4 dBW
Simulation	-55.4 dBW	-11.3 dBW	-18.8 dBW

moments, pointing out a correct rendition of the radar echoes by the simulator, at least from a statistical point of view.

2) Mare Crisium: A similar simulation was run for LRS radargram 20071227143959 of an area within Mare Crisium, Moon, where a subsurface composed of two layers was also discovered. The DEM was constructed as in the previous simulation, by stacking copies of the surface at the depths indicated in [19]. The interlayer dielectric properties were taken from those indicated in [19] ($\epsilon_1 = 4, \tan\delta_1 = 0.0035$, $\epsilon_2 = 6.61, \tan\delta_2 = 0.002$, $\epsilon_3 = 9.48$). All the other parameters are the same as in the previous simulation. Fig. (11-b) shows a shaded relief map of the surface along with the ground track of the radargram.

TABLE II
OCEANUS PROCELLARUM: STATISTICAL PROPERTIES OF THE RECORDED LAYERS

		LRS	Simulation
S0	μ	-59.2	-55.4
	σ	3.91	4.45
	γ_3	-0.47	-1.01
	γ_4	2.95	3.79
S1	μ	-72.3	-66.7
	σ	5.91	5.23
	γ_3	-1.29	-1.42
	γ_4	6.55	6.38
S2	μ	-76.6	-74.2
	σ	5.86	5.49
	γ_3	-1.04	-1.23
	γ_4	4.98	6.13

TABLE III
MARE CRISIUM: AVERAGE POWER LEVELS OF THE RECORDED LAYERS

	S0	S1-S0	S2-S0
LRS	-57.3 dBW	-11.9 dBW	-15.0 dBW
Simulation	-56.4 dBW	-10.9 dBW	-15.3 dBW

TABLE IV
MARE CRISIUM: STATISTICAL PROPERTIES OF THE RECORDED LAYERS

		LRS	Simulation
S0	μ	-57.3	-56.4
	σ	4.37	4.91
	γ_3	-0.60	-0.64
	γ_4	2.71	2.87
S1	μ	-69.2	-67.3
	σ	5.92	5.64
	γ_3	-0.89	-1.03
	γ_4	3.42	4.74
S2	μ	-72.4	-71.7
	σ	5.37	5.71
	γ_3	-1.02	-1.18
	γ_4	4.12	5.21

The result of this simulation are presented in Fig. 15. As previously, the simulator correctly reproduced the original data, taking into account the limitations already exposed, such as a lack of diffuse response. Clutter is overestimated in some areas (notably around Lat $\simeq 12.25°$N), and the subsurface layers echoes are more prominent and less discontinuous. The mounds "md1" and "md2" and the clutter sources "c1" and "c2" are correctly rendered.

The statistical properties of the echoes are also analysed. As in this LRS radargram the layers are only truly visible between Lat $\simeq 14°$N and Lat $\simeq 14.5°$N, we decided to restrict our analysis around that zone, for both the simulation and the original data. A plot of the average range-line can be seen in Fig. (13-b). Conclusions similar to those of the previous simulation can be drawn, namely, a good overall agreement, despite a lack of diffuse response due to smaller-scale roughness, making the peaks less prominent, and a slightly brighter global response. One can even notice an even better agreement in this case, likely due tot he fact we restricted our analysis to a portion where the subsurface echoes are clearly visible, instead of the whole radargram as in the previous test. The power levels of each layer are reported in table III, again with excellent agreement for S1-S0 and S2-S0, and a 1.1 dB difference for S0, the surface echo brightness. For each layer, an histogram of the echo brightness was derived (see Fig. 16), and the moments of those distributions are given in table IV. Again, an even better agreement can be observed for this restricted portion of this simulation.

B. Elysium Planitia (SHARAD)

We finally present a simulation of SHARAD radargram 0589803, recorded over Elysium Planitia, Mars, where subsurface features can be observed. As we do not apply any SAR focusing to our data, the simulations should be compared to the unfocused SHARAD data product, known as Experimental Data Record (EDR). However, the signal-to-noise ratio of this data product is insufficient to allow for meaningful comparison. The simulated radargram is thus compared to (i)

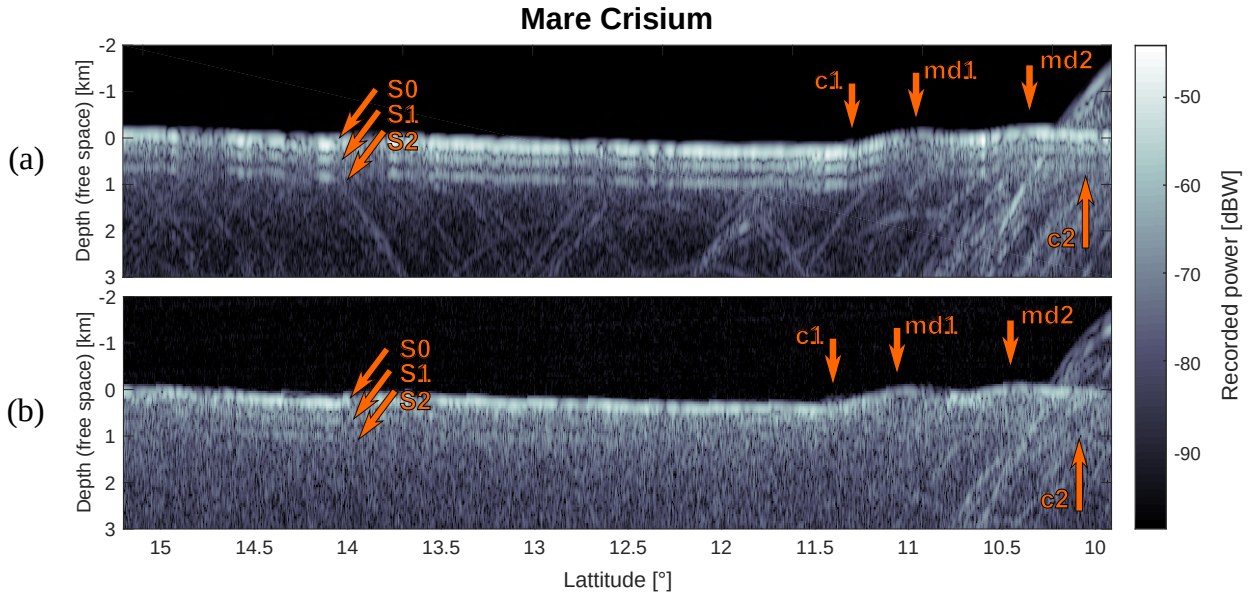

Fig. 15. Comparison between (a) simulation result and (b) LRS radargram 20071227143959 of Mare Crisium. Features of interest are labeled with arrows and are discussed in the text. "S0", "S1", and "S2" are the echoes for the surface, the first subsurface layer, and the second subsurface layer, respectively. "md1", "md2" are noteworthy geological features. "c1" and "c2" are noteworthy sources of clutter.

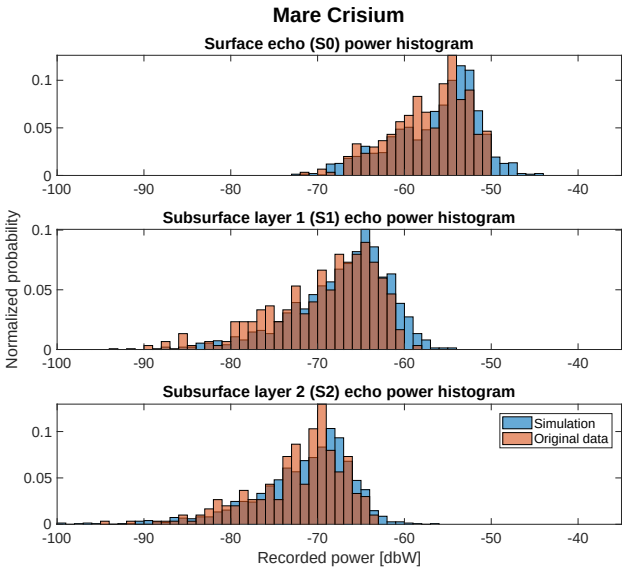

Fig. 16. Mare Crisium radagram: echo brightness histograms for all three layers. The range bin analysed in each case is the one of the corresponding peak in Fig. (13-b).

the focused data product, known as Reduced Data Record (RDR), and (ii) the incoherent SHARAD clutter simulator presented in [25]. While a proper validation is thus no longer possible, these two references images together allow to verify whether the geometry of the simulated radargram is correct. The interest of this validation simulation lies in the fact that the simulated radagram can be compared to another simulation result obtained with the same DEM.

RDR SHARAD radargrams are characterized by a free-space range resolution of 15 metres, a sampling rate of 26.67 MHz, and a PRF 700 Hz [26]. In the simulation, the PRF was reduced to 25 Hz in order to reduce the computation time. The DEM of the surface directly comes from the altimetry measurements of the MOLA instrument [28], and has a resolution of 463 metres. The subsurface was modelled by replacing the southern mound by a very smooth gradient intended to be a continuation of the underlying plain, as shown in Fig. (17). Based on the findings in [4], we set the dielectric constant of the first layer to $\epsilon_{r,1} = 3$ with $\tan\delta = 0.006$, and that of the subsurface layer to $\epsilon_{r,2} = 7$. We selected a footprint with $r = 50$ km for this simulation.

The simulation results are shown in Fig. 18. Due to SAR processing applied to the SHARAD RDR data (Fig. 18-c), only a visual comparison can be performed here. Indeed, comparing power levels between two radargrams with different processing levels is of little meaning. The subsurface layer beneath the mound at a latitude of $2.5°$N is reproduced satisfactorily, even when factoring in the uncertainties on the dielectric properties of the terrain and the fundamentally unknown nature of the subsurface DEM. The comparison between the output of the proposed simulator (Fig. 18-b) and that of the incoherent clutter simulator presented in [25] (Fig. 18-a) is an instructive exercise as both are produced using the same DEM. As far as surface clutter is concerned, the two algorithms produce very similar surface responses, with many clutter sources being easily identifiable in both images.The main difference between the two (excluding the subsurface layer) is a higher grain in the response, closer in aspect to that of actual radar data. As our method takes the signal phase into account, it is not surprising that the effects of surface roughness are better rendered, at least starting from the scale of the DEM. Moreover, the proposed simulation method also makes the rendering of the subsurface layer possible.

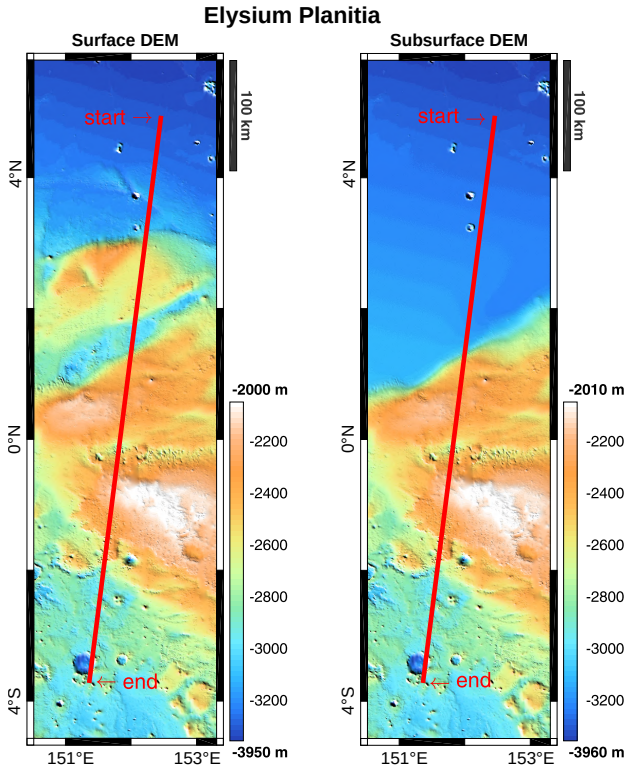

Fig. 17. Ground track the MRO probe during acquisition of SHARAD radargram 0589803 (red line) superimposed on a shaded relief map of the surface and the subsurface, an area in Elysium Planitia, Mars.

C. Computational resources

Our technique is implemented in MATLAB(R), and is parallelized in the spacecraft position (the "horizontal axis" of an usual radargram such as that of Fig. 12), meaning that it is able to compute many individual range lines simultaneously. The production of a single range line in the LRS example above, took about 16 hours on a single core of a Intel Xeon E5-2650 v3 2.3GHz CPU, with negligible RAM requirements. We additionally expect to shrink this computation time significantly by making use of GPUs alongside CPUs. Table V compares the time and RAM requirements of the proposed method against a 3D FDTD-type method for both datasets (LRS and SHARAD). The "MRS-LPA (raw DEM)" values refer to simulations using the native DEM resolution, without any resampling, as in Sec. V, whereas the "MRS-LPA (resampled)" values refer to simulations where the DEM has been resampled to have a resolution of $0.2\sqrt{\lambda h/2}$, deemed optimal for the linear phase approximation [1]. The corresponding DEM resolutions are 118.5 m and 346 m for the LRS dataset, respectively, and 463 m and 300 m for the SHARAD dataset, respectively. The "MRS-LPA (resampled)" values provide a better performance comparison with 3D-FDTD since the DEM resolutions are optimized for each method. The FDTD values are based on the equations of [15], and assume 60 CPU operations per cell. It can be seen that the proposed method is considerably faster and lighter with regard to RAM requirements. For a given simulation scene, the large numbers in FDTD methods are driven by the need to have voxel dimensions smaller than $\lambda/10$ and time-steps shorter than $10\sqrt{3}/(\lambda c)$.

TABLE V
COMPUTATIONAL RESOURCES: 3D-FDTD VS. MULTILAYER COHERENT SIMULATOR

		Time [h]	RAM [Gb]
Data set 1 (LRS)	MRS-LPA (raw DEM)	16	< 16
	MRS-LPA (resampled)	0.22	< 16
	3D-FDTD	862	1500
Data set 2 (SHARAD)	MRS-LPA (raw DEM)	0.11	< 16
	MRS-LPA (resampled)	0.52	< 16
	3D-FDTD	13794	98261

VI. CONCLUSION

In this paper, we have presented a coherent multilayer radargram simulator based on the linear phase approximation method for computing the facet phase. The proposed algorithm is able to treat target areas with a subsurface presenting an arbitrary number of layers in a coherent way, with a good accuracy and much lower computational costs than 3D-FDTD methods. This is possible due to a set of approximation introduced in the simulation technique. We have performed a thorough validation against two existing LRS radargrams and demonstrated the versatility of the tool by reproducing an unfocused SHARAD radargram.

The most important of the approximations used is that the signals propagating into the subsurface are considered to be plane waves. While this choice makes the algorithm computationally rather light, it might induce inaccuracies on the phase, and might lead to miss some echoes. Indeed, for any wave hitting a given triangle, only one transmitted and reflected wavevector is computed. In reality, diffraction effects will lead to a more complicated picture, and several such wavevectors should be generated at each interface (ideally, a continuum of them). We believe that the reason this approximation is acceptable for real-life terrains, as indicated by the results in this paper, is that their natural roughness induces a degree of randomization to the phase, making phase errors less relevant. Another simplifying assumption used in this method is to consider that those plane waves impact their target triangle on their incentre (rather than on the actual impact point, which can be elsewhere on the triangle). The results shown in Sec. V show that the delay and phase inaccuracies that ensue are minor, as the subsurface echoes show no unexpected behaviour in either of the three tested cases.

A first limitation of our proposed method is the choice to only consider the central frequency of the radar (rather than all the frequencies of the emitted chirp) in the application of the Stratton-Chu integral, which might lead to inaccuracies for radars with very high fractional bandwidths. Secondly, double reflection aren't taken into account. However, this is a problem mostly for airborne radar platforms, and is not critical for orbital sounders, which are the focus of our work.

However, implementing both a fully-rigorous way to calculate subsurface propagation and the capability to simulate double reflections would likely make our simulator computationally very demanding. Consequently, we believe that the good agreement between our simulation results and existing

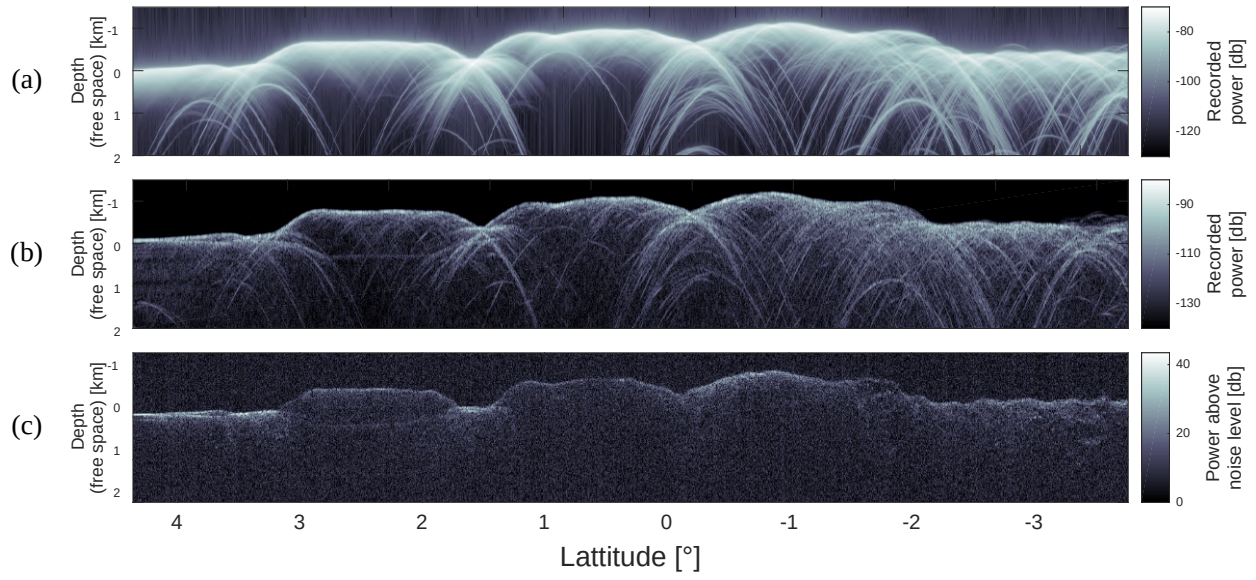

Fig. 18. (a) Incoherent clutter simulation. (b) Simulation result using the proposed method. (c) RDR SHARAD radargram 0589803.

radar data (see Sec. V) allows us to consider the proposed method as a good trade-off between accuracy and computational efficiency.

The experimental results of Sec. V also demonstrate the potential in using the simulator to test subsurface hypotheses, showing for instance, if a particular drop in the subsurface power is due to a change in subsurface properties or simply a consequence of the scattering geometry.

As a final remark, we point out that due to the finite resolution of the available DEMs (118.5m for LRS simulations and 463m for the SHARAD simulation), the algorithm does not model the small-scale roughness of the terrain, which causes a deficit in the diffuse response of the simulated radargrams with respect to the original data. To add a diffuse response to the algorithm in a rigorous way is deferred to a future study.

ACKNOWLEDGMENT

The authors would like to thank Yann Berquin and Alain Herique for their advice and the fruitful discussions, as well as Simon Yueh and all anonymous reviewers, whose comments helped dramatically improve the quality of the paper. This work was supported by the Italian Space Agency partially under Contract ASI/INAF n. 2013-056-R.O "Partecipazione italiana alla fase A/B1 della missione JUICE" and partially under the contract ASI n. 2016-14-U.O "SaTellite Radar sounder for eArTh sUb-surface Sensing (STRATUS)".

REFERENCES

[1] Yann Berquin, Alain Herique, Wlodek Kofman, and Essam Heggy. Computing low-frequency radar surface echoes for planetary radar using huygens-fresnel's principle. *Radio Science*, 50(10):1097–1109, 2015. 2015RS005714.

[2] Donald D Blankenship, Duncan A Young, William B Moore, and John C Moore. Radar sounding of europas subsurface properties and processes: The view from earth. *Europa. University of Arizona Press, Tucson, AZ*, 2009.

[3] L. Bruzzone, G. Alberti, C. Catallo, A. Ferro, W. Kofman, and R. Orosei. Subsurface radar sounding of the jovian moon ganymede. *Proceedings of the IEEE*, 99(5):837–857, May 2011.

[4] Lynn M Carter, Bruce A Campbell, Thomas R Watters, Roger J Phillips, Nathaniel E Putzig, Ali Safaeinili, Jeffrey J Plaut, Chris H Okubo, Anthony F Egan, Roberto Seu, et al. Shallow radar (sharad) sounding observations of the medusae fossae formation, mars. *Icarus*, 199(2):295–302, 2009.

[5] WenZhe Fa and YaQiu Jin. Simulation of radar sounder echo from lunar surface and subsurface structure. *Science China Earth Sciences*, 53(7):1043–1055, 2010.

[6] A. Ferro, A. Pascal, and L. Bruzzone. A novel technique for the automatic detection of surface clutter returns in radar sounder data. *IEEE Transactions on Geoscience and Remote Sensing*, 51(5):3037–3055, May 2013.

[7] Essam Heggy, Giovanni Scabbia, Lorenzo Bruzzone, and Robert T. Pappalardo. Radar probing of jovian icy moons: Understanding subsurface water and structure detectability in the {JUICE} and europa missions. *Icarus*, 285:237 – 251, 2017.

[8] Florence Hélière, Chung-Chi Lin, Hugh Corr, and David Vaughan. Radio echo sounding of pine island glacier, west antarctica: Aperture synthesis processing and analysis of feasibility from space. *IEEE Transactions on Geoscience and Remote Sensing*, 45(8):2573–2582, 2007.

[9] C. C. Hernandez, V. Krozer, J. Vidkjaer, and J. Dall. Polaris: Esa's airborne ice sounding radar front-end design, performance assessment and first results. In *2009 IEEE MTT-S International Microwave Symposium Digest*, pages 393–396, June 2009.

[10] Ya A Ilyushin, R Orosei, O Witasse, and B Sánchez-Cano. Clusim: A synthetic aperture radar clutter simulator for planetary exploration. *Radio Science*, 52(9):1200–1213, 2017.

[11] John David Jackson and Ronald F Fox. Classical electrodynamics. *American Journal of Physics*, 67(9):841–842, 1999.

[12] Takao Kobayashi, Hiroshi Oya, and Takayuki Ono. A-scope analysis of subsurface radar sounding of lunar mare region. *Earth, planets and space*, 54(10):973–982, 2002.

[13] Takao Kobayashi, Hiroshi Oya, and Takayuki Ono. B-scan analysis of subsurface radar sounding of lunar highland region. *Earth, planets and space*, 54(10):983–991, 2002.

[14] Jin Au Kong. Theory of electromagnetic waves. *New York, Wiley-Interscience, 1975. 348 p.*, 1975.

[15] Karl S Kunz and Raymond J Luebbers. *The finite difference time domain method for electromagnetics*. CRC press, 1993.

[16] Chuan Liu, Hongxia Ye, and Ya-Qiu Jin. Simulation of radar echoes from mars' surface/subsurface and inversion of surface media parameters. *Radio Science*, 49(7):473–484, 2014.

[17] J.-F. Nouvel, A. Herique, W. Kofman, and A. Safaeinili. Radar signal simulation: Surface modeling with the facet method. *Radio Science*, 39(1):n/a–n/a, 2004. RS1013.

[18] T. Ono, A. Kumamoto, Y. Kasahara, Y. Yamaguchi, A. Yamaji, T. Kobayashi, S. Oshigami, H. Nakagawa, Y. Goto, K. Hashimoto, Y. Omura, T. Imachi, H. Matsumoto, and H. Oya. The lunar radar sounder (lrs) onboard the kaguya (selene) spacecraft. *Space Science Reviews*, 154(1):145–192, 2010.

[19] Takayuki Ono, Atsushi Kumamoto, Hiromu Nakagawa, Yasushi Yamaguchi, Shoko Oshigami, Atsushi Yamaji, Takao Kobayashi, Yoshiya Kasahara, and Hiroshi Oya. Lunar radar sounder observations of subsurface layers under the nearside maria of the moon. *Science*, 323(5916):909–912, 2009.

[20] Claudio Papa, Giovanni Alberti, Giuseppe Salzillo, Gianfranco Palmese, Dario Califano, L Ciofaniello, Maria Daniele, Claudia Facchinetti, Francesco Longo, Roberto Formaro, et al. Design and validation of a multimode multifrequency vhf/uhf airborne radar. *IEEE Geoscience and Remote Sensing Letters*, 11(7):1260–1264, 2014.

[21] G. Picardi, D. Biccari, R. Seu, L. Marinangeli, W.T.K. Johnson, R.L. Jordan, J. Plaut, A. Safaenili, D.A. Gurnett, G.G. Ori, R. Orosei, D. Calabrese, and E. Zampolini. Performance and surface scattering models for the mars advanced radar for subsurface and ionosphere sounding (marsis). *Planetary and Space Science*, 52(13):149 – 156, 2004. Exploring Mars Surface and its Earth Analogues.

[22] Paolo Rocca, Nicola Anselmi, and Andrea Massa. Interval arithmetic for pattern tolerance analysis of parabolic reflectors. *IEEE Transactions on Antennas and Propagation*, 62(10):4952–4960, 2014.

[23] Fernando Rodriguez-Morales, Sivaprasad Gogineni, Carlton J Leuschen, John D Paden, Jilu Li, Cameron C Lewis, Benjamin Panzer, Daniel Gomez-Garcia Alvestegui, Aqsa Patel, Kyle Byers, et al. Advanced multifrequency radar instrumentation for polar research. *IEEE Transactions on Geoscience and Remote Sensing*, 52(5):2824–2842, 2014.

[24] MA Rosenburg, Oded Aharonson, JW Head, MA Kreslavsky, E Mazarico, Gregory A Neumann, David E Smith, Mark H Torrence, and Maria T Zuber. Global surface slopes and roughness of the moon from the lunar orbiter laser altimeter. *Journal of Geophysical Research: Planets*, 116(E2), 2011.

[25] F. Russo, M. Cutigni, R. Orosei, C. Taddei, R. Seu, D. Biccari, E. Giacomoni, O. Fuga, and E. Flamini. An incoherent simulator for the sharad experiment. In *2008 IEEE Radar Conference*, pages 1–4, May 2008.

[26] R. Seu, D. Biccari, R. Orosei, L.V. Lorenzoni, R.J. Phillips, L. Marinangeli, G. Picardi, A. Masdea, and E. Zampolini. Sharad: The {MRO} 2005 shallow radar. *Planetary and Space Science*, 52(13):157 – 166, 2004. Exploring Mars Surface and its Earth Analogues.

[27] Seelig Sinton and Yahya Rahmat-Samii. Random surface error effects on offset cylindrical reflector antennas. *IEEE transactions on antennas and propagation*, 51(6):1331–1337, 2003.

[28] David E Smith, Maria T Zuber, Sean C Solomon, Roger J Phillips, James W Head, James B Garvin, W Bruce Banerdt, Duane O Muhleman, Gordon H Pettengill, Gregory A Neumann, et al. The global topography of mars and implications for surface evolution. *Science*, 284(5419):1495–1503, 1999.

[29] M.G. Spagnuolo, F. Grings, P. Perna, M. Franco, H. Karszenbaum, and V.A. Ramos. Multilayer simulations for accurate geological interpretations of {SHARAD} radargrams. *Planetary and Space Science*, 59(1112):1222 – 1230, 2011. Geological Mapping of Mars.

[30] Fawwaz T Ulaby, Richard K Moore, and Adrian K Fung. Microwave remote sensing active and passive. 2015.